Applied Surface Science 543 (2021) 148824

Contents lists available at ScienceDirect

Applied Surface Science

journal homepage: www.elsevier.com/locate/apsusc

Full Length Article

A novel amino phosphonate-coated magnetic nanoparticle as MRI contrast agent

Davino M.A. Neto [a,b], Luelc S. da Costa [c], Fernando L. de Menezes [b], Lillian M.U.D. Fechine [b], Rafael M. Freire [d,e], Juliano C. Denardin [e], Manuel Bañobre-López [f], Igor F. Vasconcelos [g], Thiago S. Ribeiro [g], Luzia Kalyne A.M. Leal [h], João A.C. de Sousa [h], Juan Gallo [f], Pierre B. A. Fechine [b,*]

[a] Federal Institute of Education, Science and Technology of Ceará, Campus Camocim, Zip Code 62400-000 Camocim, CE, Brazil
[b] Group of Chemistry of Advanced Materials (GQMat), Department of Analytical Chemistry and Physic-chemistry, Federal University of Ceará, Campus do Pici, Zip Code 60451-970 Fortaleza, CE, Brazil
[c] Institute of Chemistry, States University of Campinas (UNICAMP), Campinas, SP 13083-970, Brazil
[d] Institute of Applied Chemical Sciences, Universidad Autónoma de Chile, Santiago 8910060, Chile
[e] Department of Physics, Universidad de Santiago de Chile, USACH, Av. Ecuador 3493, Santiago, Chile
[f] Advanced (magnetic) Theranostic Nanostructures Lab, International Iberian Nanotechnology Laboratory, Av. Mestre José Veiga s/n, Zip Code 4715-330 Braga, Portugal
[g] Department of Metallurgic and Materials Engineering, Federal University of Ceará – UFC, Campus do Pici, Zip Code 60451-970 Fortaleza, Brazil
[h] Department of Pharmacy, Federal University of Ceará, Rua Alexandre Baraúna, 949, Zip Code 60430-160 Fortaleza, Brazil

ARTICLE INFO

Keywords:
Amino-phosphonate
Functionalized magnetic nanoparticles
MRI contrast agent
Sonochemistry

ABSTRACT

The great performance of functionalized Fe_3O_4 nanoparticles (NPs) as contrast agent for magnetic resonance imaging (MRI) is related to the functionalizing agents, once can tune colloidal properties, chemical stability, hydrophilicity, overall toxicity, as well as, dipole interparticle interactions. Phosphonate derivatives have proven to be excellent capping agents due to their ability to control the above parameters. However, the available functionalizing agents do not provide enough both attached and free-form phosphoric acid groups on NPs surface. Herein, we report the use of a commercially available amino-phosphonate compound, diethylenetriaminepenta (methylene phosphonic acid, DTPMP), to functionalize Fe_3O_4 NPs to be potentially applied as MRI contrast agent. For the synthesis of DTPMP-coated Fe_3O_4 NPs, two methodologies were applied, hydrothermal and sonochemical approaches. Several characterization techniques were performed, confirming the success of surface functionalization, which allowed a deep chemical discussion involving the interactions between DTPMP and Fe_3O_4 NPs. Furthermore, relaxivity and cytotoxicity analyses confirmed the MRI contrast agent potential of the DTPMP-coated Fe_3O_4 NPs, presenting non-cytotoxicity profile and high values of transverse relaxivity (357–417 mM^{-1} s^{-1}). Therefore, this work presents a novel and excellent alternative magnetic material for biological and technological application, mainly considering MRI contrast agent.

1. Introduction

Magnetic resonance imaging (MRI) is a noninvasive, nonionizing, and radiation-free imaging technique, which has been applied in diagnosis and prognosis of several diseases [1]. MRI image obtention is based on the contrast generated between health and diseased tissues, promoted by a chemical-based contrast agent that the shortening relaxation times of water protons leads to an enhancement of the tissues contrast [2]. Magnetic nanoparticles (MNPs) have been emerged as a great MRI contrast agents, which introduce new possibilities into biomedical research and clinical diagnosis [3–6].

For this proposal, MNPs must follow some additional requisites, such as good colloidal stability at physiological salt concentrations and at different pH levels to enable intravenously administration [7,8]. Therefore, MNPs have been surface-modified with capping agents in order to prevent their aggregation into human body, and also decrease

* Corresponding author.
E-mail address: fechine@ufc.br (P.B.A. Fechine).

https://doi.org/10.1016/j.apsusc.2020.148824
Received 16 October 2020; Received in revised form 24 November 2020; Accepted 20 December 2020
Available online 24 December 2020

overall cytotoxicity. Indeed, surface modification can modulate the behavior of MNPs in physiological medium, improving biocompatibility and hydrophilicity [9,10]. For instance, functionalizing agents can rearrange the atoms on MNPs surface, affecting the magnetic field inhomogeneity and playing an essential role regarding water molecules interactions [11]. Therefore, the performance of MNPs as MRI contrast agent is also tailored by the chosen of an excellent capping agent.

According to literature, several functionalizing agents can be found for MRI applications, which these compounds promote hydroxyl, carboxylic acids or amine groups in order to interact with external working environment [3,9,11]. Generally, capping agents are based on polyethylene glycol (PEG) [12,13] and dextran [14]; polyacrylic acid [15]; carboxymethyl cellulose [16], carboxyl-functionalized PEG [17] and citrate [18]; and chitosan [19] and polyethylenimine (PEI) [20]. Catechol-based capping agents are also used, however they do not interact directly to the working environment [21,22].

Another class of functionalizing agent is based on phosphonate molecules, mainly due to the strong affinity of phosphate/phosphoric acid groups to Fe atoms on MNPs surface [23], where phosphonate derivatives can promote better chemical stability against hydrolysis, pH variations, dilutions and oxidation [24]. Therefore, phosphonate-based functionalizing agents have been used in surface post-modification of MNPs, once phosphonate groups can act as a crosslinking between MNPs surface and functionalizing agent molecule [25–28]. For instance, Torrisi *et al.* synthesized phosphonic acid poly(ethylene glycol) copolymers to coat MNPs, in which the phosphonate groups are attached to Fe atoms on inner MNPs surface, whereas polyethylene glycol lengths is on the outer of surface boundary [27]. However, external phosphonate surface groups provide interesting features, such as: a) interaction with rare earth elements, which could generate a more versatile profile to MNPs application [13,25–28]; b) bone affinity property for diagnostic of bone-related pathologies [29]; c) concerning application as contrast agent for MRI, phosphonate groups promote an enhancement in relaxivity through second sphere effects due to strong hydrogen bonding interaction with water molecules [30,31]. Besides outstanding versatility of phosphonate-based molecules application, their use as functionalizing agents on magnetic nanoparticles still limited.

Therefore, in this work, we propose an amino phosphonate-functionalized Fe_3O_4 NPs, using diethylenetriaminepenta (methylene phosphonic acid, DTPMP) (Scheme 1A) as capping agent. Recently, DTPMP has been used to study sodium sulfate crystallization [32], preparing hollow Co-DTPMP complexes to be used as Fenton catalysts [33], radioanalytical separation [34] and corrosion inhibitor [35]. DTPMP has also been used as chelating agent for gadolinium (Gd^{3+}) to be applied as contrast agent in calcified tissues [36]. The authors reported that the complex DTPMP-Gd^{3+} exhibited high bone affinity and renal clearance [36]. Herein, we truly believe that this molecule is a good candidate as functionalizing agent due to the following reasons: a) it is a commercially available compound with a relative low price; b) its molecular arrangement allows both attached and free-form phosphoric acid groups on MNPs surface, offering an enhanced chemical and colloidal stability, hydrophilic surface, as well as a tunable post-modification profile; c) the presence of both amine and phosphoric acid groups can generate a amphoteric surface, where, depending on the pH of the medium, gives a positive or negative surface charge. Therefore, the proposed phosphonate-based nanomaterial presents a versatile profile for MRI and other technological applications, such as sensing formulations, catalysis, separation science and biological areas [37]. Although, to the best of our knowledge, no study has been reporting functionalization process on MNPs using DTPMP.

Concerning performance of functionalized MNPs, the synthetic methodology plays a key role regarding material properties and structure [38], which it can be modulated according to final application. Herein, sonochemistry has drawn much attention of the scientific community mainly due to cavitation phenomenon, which provides a unique environment reaction with hot spots in the range of 5000 K and pressures higher than 1000 atm [39]. Remarkably, our group has been developed advanced nanomaterials by sonochemistry approach for different applications, such as electrochemical sensor [40], sunscreen formulation [41] and MRI contrast agent [42]. Recently, we developed a fast ultrasound-assisted method, around 12 min, to prepare MNPs functionalized with sodium polyacrylate, trisodium citrate, branched polyethylenimine and sodium oleate, which exhibited excellent magnetic, colloidal, and relaxivity properties for MRI application.

Therefore, the main propose of this study was to synthesize a novel ultrasound-assisted hybrid nanomaterial with great performance as MRI contrast agent, and also compare sonochemical and hydrothermal methods regarding time reaction and final material properties. Herein, the overall DTPMP-functionalized Fe_3O_4 NPs characterization was achieved through a combination of techniques to precisely describe structure, morphology and magnetic properties of MNPs, as well as particles colloidal stability in aqueous medium and cytotoxicity. Finally, the MNPs were evaluated as MRI contrast agent, which also showed great potential to be applied in other biological and technological applications.

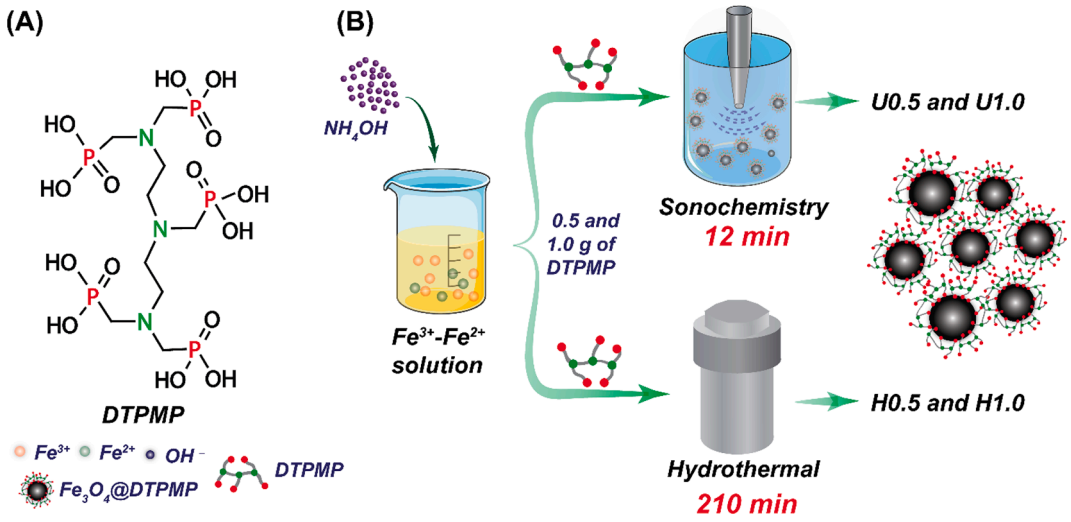

Scheme 1. (A) Structure of DTPMP. (B) Chemical routes to synthesize DTPMP-coated MNPs.

2. Materials and methods

2.1. Materials

Iron chloride (III) hexahydrate ($FeCl_3{\cdot}6H_2O$) and iron sulfate heptahydrate ($FeSO_4{\cdot}7H_2O$) were purchased from Vetec Química, Brazil. Diethylenetriaminepenta (methylene phosphonic acid) – (DTPMP, Scheme 1A) 50% (T) was purchased from Sigma–Aldrich and used as received. Ammonium hydroxide (29%) (NH_4OH) was purchased from Dinâmica Química, Brazil. All other reagents were used as received without any further purification.

2.2. Synthesis of DTPMP-functionalized Fe_3O_4 NPs

The DTPMP-coated NPs were synthesized by two methodologies, sonochemistry and hydrothermal approach. For each pathway, two stoichiometries of functionalizing agent, 0.5 g and 1.0 g of DTPMP, were tested (Scheme 1B).

2.2.1. Sonochemistry procedure

DTPMP-based MNPs were synthesized according to ultrasound-assisted method developed in our group [42], using an ultrasound equipment (Q500 Sonicator - Qsonica) with a microtip probe of 3.2 mm under sonication conditions of 200 W and pulse-regime of *3s on* and *1s off*. Briefly, 1.0 g (3.6 mmol) of $FeSO_4{\cdot}7H_2O$ and 1.9 g (7 mmol) of $FeCl_3{\cdot}6H_2O$ were dissolved in 15 mL of deionized water. This obtained solution was heated up until reached 60 °C (~3 min) and further sonicated during 1 min under already described sonication conditions. Subsequently, 10 mL of concentrated NH_4OH solution were added under sonication for 4 min. Then, 4 mL of a solution containing a certain amount of DTPMP (see below) was added into reaction mixture, allowing sonication in the last 4 min.

For sample containing 0.5 g of DTPMP, the solution of DTPMP was prepared by adding 0.6 mL of DTPMP in 3.4 mL of deionized water. For sample with 1.0 g of DTPMP, 1.2 mL of concentrated DTPMP were added in 2.8 mL of deionized water. Additionally, in order to remove the excess of NH_4OH and unbounded DTPMP molecules, the obtained particles were washed with 30 mL deionized water followed by magnetic decantation (3 times). Furthermore, the NPs were dialyzed until neutral pH. Finally, the samples were centrifuged for 10 min at 3000 rpm to remove large aggregates.

This procedure generated two samples labeled as U0.5 and U1.0, which correspond to ultrasound-assisted Fe_3O_4 NPs with 0.5 g and 1.0 g of DTPMP, respectively, as shown in Scheme 1B. It was also prepared uncoated Fe_3O_4 NPs by the same methodology, which was labeled as Fe_3O_4-U.

2.2.2. Hydrothermal

For hydrothermal approach, an adapted methodology was followed according to Kolen'ko *et al.* [43]. Firstly, 3.80 g (14 mmol) of $FeCl_3{\cdot}6H_2O$ and 2.05 g (7 mmol) of $FeSO_4{\cdot}7H_2O$ were dissolved in 38 mL of deionized water, and further added into a 90 mL of poly(tetrafluoroethylene) (PTFE) vessel. Then, 20 mL of NH_4OH were added to the obtained solution, followed by addition of a certain amount (see below) of concentrated DTPMP. Then, the PTFE reactor was closed and sealed in a stainless steel autoclave, which was kept at 150 °C for 3.5 h (See Scheme 1B). For sample with 0.5 g and 1.0 g of DTPMP, 0.6 mL and 1.2 mL of concentrated DTPMP was used, respectively.

For hydrothermal particles, the purification step was similar to one described for sonochemistry approach. Hydrothermal procedure generated two samples labeled as H0.5 and H1.0, which correspond to Fe_3O_4 NPs prepared by hydrothermal method with addition of 0.5 g and 1.0 g of DTPMP, respectively (Scheme 1B). Uncoated Fe_3O_4 NPs obtained by hydrothermal methodology were labeled as Fe_3O_4-H.

2.2.3. Complex DTPMP-Fe^{2+}-Fe^{3+}

In order to evaluate the interactions between DTPMP molecules and Fe atoms on the surface of Fe_3O_4 NPs, a complex of DTPMP and Fe^{2+}–Fe^{3+} cations was synthesized. Briefly, 1.34 g (4.9 mmol) of $FeCl_3{\cdot}6H_2O$ and 1.35 g (4.9 mmol) of $FeSO_4{\cdot}7H_2O$ were dissolved in 8 mL of deionized water. Then, 1.0 mL of concentrated DTPMP was added, which it was observed the formation of a light yellowish precipitate. The mixture remained under magnetic stirring for 30 min. To remove the unbounded iron cations, the precipitate was washed with 30 mL of deionized water followed by centrifugation (2000 rpm for 5 min). The precipitate was dried under vacuum for further characterizations.

2.3. Characterization of DTPMP-functionalized Fe_3O_4 NPs

X-ray diffraction (XRD) analysis were performed using an X'Pert MPD X-ray powder diffractometer (PANalytical, Westborough, United States) with 40 kV and 30 mA in a scanning range of $2\theta = 20–80°$ equipped with a Co Kα tube. The diffraction patterns were obtained using a Bragg–Brentano geometry in the continuous mode with a speed of 0.5°/min and step size of 0.02° (2θ). The Rietveld structure refinement was used to interpret and analyze the diffraction data using the program DBWstools [44]. The full-width at half maximum (FWHM) of the instrument was calculated with the standard hexaboride lanthanum. The crystallite size of each sample was calculated using Scherrer's equation.

Transmission electron microscopy (TEM) images were obtained with a MSC JEOL TEM-2100 200 kV microscope, equipped with a CCD (TVip–16 MP) and TV (Gatan ES500W) available from LNNano, Campinas, Brazil. TEM samples were dispersed in isopropyl alcohol and deposited in a drop onto carbon-coated copper grids. Subsequently, the deposited samples were allowed to dry completely overnight before analysis. The size distribution curves were obtained by manually size measuring of 150 particles [45], using the software ImageJ (U.S. National Institutes of Health, Bethesda, MD). The polydispersity index for TEM analysis (PDI_{TEM}) was calculated as reported in literature [46]. The coating thickness distribution curves were obtained by manually thickness measuring of 25 particles using ImageJ software. The data were determined measuring the distance from an imaginary plane, perpendicular to nanoparticle surface, to the end of the coating in the core-shell interface of the nanoparticle.

Mössbauer spectroscopy (MS) data were recorded at room temperature (300 K) with a FAST (ConTec) Mössbauer system spectrometer using the transmission geometry. A ^{57}Co radioactive source was used. The data analysis was performed using the NORMOS program written by R. A. Brand (distributed by Wissenschaftliche Elektronik GmbH, Germany). The isomer shifts (δ) relative to α-Fe were found at room temperature.

Vibrating sample magnetometer (VSM) measurements at 300 K were recorded on a superconducting quantum interference device SQUID-VSM magnetometer from Quantum Design. Prior to the measurements, the particles were dried overnight in vacuum at room temperature, ground using an agate mortar, and finally placed in gelatin capsules for the measurements. Hysteresis loops were obtained at 300 K by applying a magnetic field up to ±20 kOe. Zero-field-cooling (ZFC) and field-cooling (FC) curves were obtained also in dried samples using the Vibrating Sample Magnetometer Mini 5T from Cryogenic Ltd. In order to obtain additional information concerning the blocking temperature (T_B) distribution of the NPs, it was applied the methodology of Bruvera *et al.* [47] on our ZFC-FC data.

The presence of DTPMP molecules on the surface of the NPs was studied by Fourier transform infrared spectroscopy (FTIR). The spectra were recorded using a Shimadzu model 8300 spectrophotometer. The samples were grounded in an agate mortar and pressed into KBr discs. The range used was 4000–400 cm^{-1}, with a resolution of 2 cm^{-1} and 128 scans.

Chemical surface analyses of the nanoparticles were carried out in a

K-Alpha X-ray photoelectron spectrometer (XPS) (Thermo Fisher Scientific, United Kingdom) equipped with a hemispherical electron analyzer and an aluminum anode ($K\alpha$ = 1486.6 eV) as X-ray source. Measurements of the DTPMP-coated NPs were carried out by using charge compensation during the analyses, and the pressure of the chamber was kept below 2×10^{-8} mbar. Survey (i.e., full-range) and high-resolution spectra were recorded using pass energies of 1 and 0.1 eV, respectively. The spectrum fitting was performed by assuming a mixed Gaussian/Lorentzian peak shape (the ratio of the Gaussian to Lorentzian form was 0.4). For the fitting of the samples U0.5, U1.0, H0.5 and H1.0 the same FWHM values as the values obtained for the samples Fe_3O_4-U and DTPMP-Fe^{2+}-Fe^{3+} were used. The X-ray photoelectron spectra presented here are the result of the average of three spectra collected at three different regions for each sample.

The hydrodynamic size of the NPs in colloidal dispersion was measured in dynamic light scattering (DLS) experiments using a Malvern Zetasizer NS 3601 at 25 °C. The DLS measurements were performed on a diluted dispersion of the NPs (~0.066 mg/mL), with a single scattering angle of 173°. The hydrodynamic size of the synthesized samples was further analyzed using phosphate buffers at pH 7.4 (PB 7.4) and PB at different salt concentration (PBS 7.4). The size estimated by DLS was expressed as Z-average values, and the polydispersity index (PDI_{DLS}) values were calculated using the cumulate method. Five measurements were performed for each sample. The zeta potential (ζ) of each sample was measured using the same instrument at 25 °C. Furthermore, measurements of hydrodynamic size and ζ at different pH values were performed using the MPT-2 Titrator device (Malvern Instruments). For the adjustment of the pH during the experiments the following solutions were used: NaOH 0.25, 0.01 mol L^{-1} and HCl 0.25 mol L^{-1}.

2.4. Toxic evaluation of the DTPMP-functionalized NPs on human neutrophils

2.4.1. Isolation of human neutrophils

Human leucocyte-rich blood from healthy adults was obtained from HEMOCE (blood bank), Fortaleza, Brazil. Polymorphonuclear cells were isolated by the Lucisano and Mantovani's method [48] with slight modifications [49], and the obtained cells suspension (80–90% neutrophils) showed 90 ± 2.0% of viability, stablished by the exclusion with Trypan blue method. The methods were carried out in accordance with the approved guidelines and Ethics Committee on Human Research (CAAE no. 18398819.2.0000.5054).

2.4.2. LDH activity test

The neutrophils suspension was incubated at 37 °C for 15 min with Hanks' solution (the medium, non-treated group), water (vehicle, control group), Triton X-100 (0.2%, cytotoxic standard) and samples U0.5; U1.0; H0.5 and H1.0 (100, 50 and 10 μg/mL). After incubation, the tubes were placed in a centrifuge at 4 °C for 10 min. Then, the supernatant of each sample was collected and maintained at low temperature to perform the absorbance measurement. The LDH activity was determined according to the LDH Liquiform kit Labtest (LDH Liquiform of Labtest Diagnostica, Lagoa Santa, MG, Brazil), where it was calculated using the following equation:

$$A = [(A_1 - A_2)/2] \times 1746.03 \quad (1)$$

where: A = LDH enzymatic activity (U/L); A_1 = absorbance at 1 min; A_2 = absorbance at 3 min and 1746.03 is the current factor calculated by the manufacturer.

2.4.3. MTT test

Human neutrophils were exposed to the sample U1.0 (10, 50 and 100 μg/mL), water (vehicle, control), Hanks' balanced salt solution (HBSS) (culture medium, negative control) or Triton X-100 (0.2%, cytotoxic standard) for 15 min at 37 °C, followed by addition of 200 μL of 3-(-4,5-dimethyl-2-thiazolyl)-2,5-diphenyl-2H-tetrazolium bromide (MTT). After 3 h of incubation with MTT, the cells were washed with phosphate buffer solution, and the Dimethyl sulfoxide (DMSO) (100 μL) was added for the solubilization of the formazan products. The absorbance was measured at 540 nm [50].

For both tests, the results are expressed as mean ± standard error of the mean (S.E.M.). The statistical significance of differences between groups was determined by One-Way anova, followed by Tukey for multiple comparisons as a post hoc test. The significance level was set at $p < 0.05$.

2.5. Relaxivity measurements and MRI-weighted images

Five aqueous dilutions with different nanoparticle concentrations (between 0 and 0.16 mM Fe) were prepared for each sample, using an aqueous solution of agar 0.5% (w/v) as solvent aiming to simulate MRI signals from human tissues. 200 μL aliquots of each dilution were measured in a mini spec mq60 contrast agent analyzer from Bruker at 37 °C and under 1.41 T magnetic field, using Carr Purcell Meiboom Gill (CPMG) sequence for transverse relaxation time (T_2) calculations. The transverse relaxivity constant (r_2) were calculated as the slope of the curve obtained by fitting the T_2^{-1} values versus the Fe concentration (mM). The Fe concentrations of the solutions were calculated using an inductively coupled plasma-optical emission spectroscopy (ICP-OES) analyzer (Shimadzu ICPE-9000).

MR phantom imaging was performed in a 3 T horizontal bore MR Solutions Benchtop (Guildford, U.K.) equipped with 48 G cm^{-1}actively shielded gradients. For imaging the samples, a 56 mm diameter quadrature bird-cage coil was used in transmit/receive mode. For the phantom measurements, the samples at different concentrations (between 25 and 150 μM in Fe) were dissolved in 200 μL of Milli-Q water a placed in custom-printed PLA holders. All MR images of the phantoms were acquired with an image matrix 256 × 252, field of view (FOV) 60 × 60 mm, three slices with a slice thickness of 1 mm, and 1 mm slice gap. For T_2-weighted imaging, a fast spin echo (FSE) sequence with the following parameters was used: T_E = 14 ms, T_R = 3000 ms, N_A = 15, A_T = 47 m 25 s. T_2 maps were acquired using multi-echo multi-slice (MEMS) sequences with the following parameters: T_E = 15 ms, T_R = 1400 ms, N_A = 10, A_T = 44 m 55 s. Post-processing was performed using ImageJ software. T_2 maps were reconstructed using following the standard equation: $S_n = S_0\,[1 - \exp\,(TE \times n/T_2)]S_n = S_0\left(1 - e^{TEn/T_2}\right)$, where S is the signal intensity, TE is the echo time and T_2 is relaxation time.

3. Results

After DTPMP-coated MNPs synthesis, a full characterization analysis was performed in order to evaluate the success of the DTPMP functionalization and its impact on the structural (XRD and MS), magnetic (VSM and ZFC-FC) and colloidal (DLS) properties of the MNPs. Furthermore, FT-IR and XPS chemically showed how DTPMP molecules are binding on MNPs surface. In addition, we evaluated its potential to be applied as contrast agent in MRI through cytotoxicity experiments, relaxivity measurements and weighted MR images.

3.1. Structure and magnetic properties

3.1.1. XRD

XRD patterns for the synthesized MNPs are shown in Fig. 1A. Data from the Rietveld structural refinement are shown in Table 1. Both the percentage of errors (R_{WP}) and goodness of fitting (S) values were found to be in agreement with those of a high-quality refinement (data not shown) [51]. The analysis of the position and intensity of the diffraction peaks confirmed that all synthesized MNPs samples are composed of a single crystalline phase with a spinel structure *Fd3m* (ICSD code: 84611)

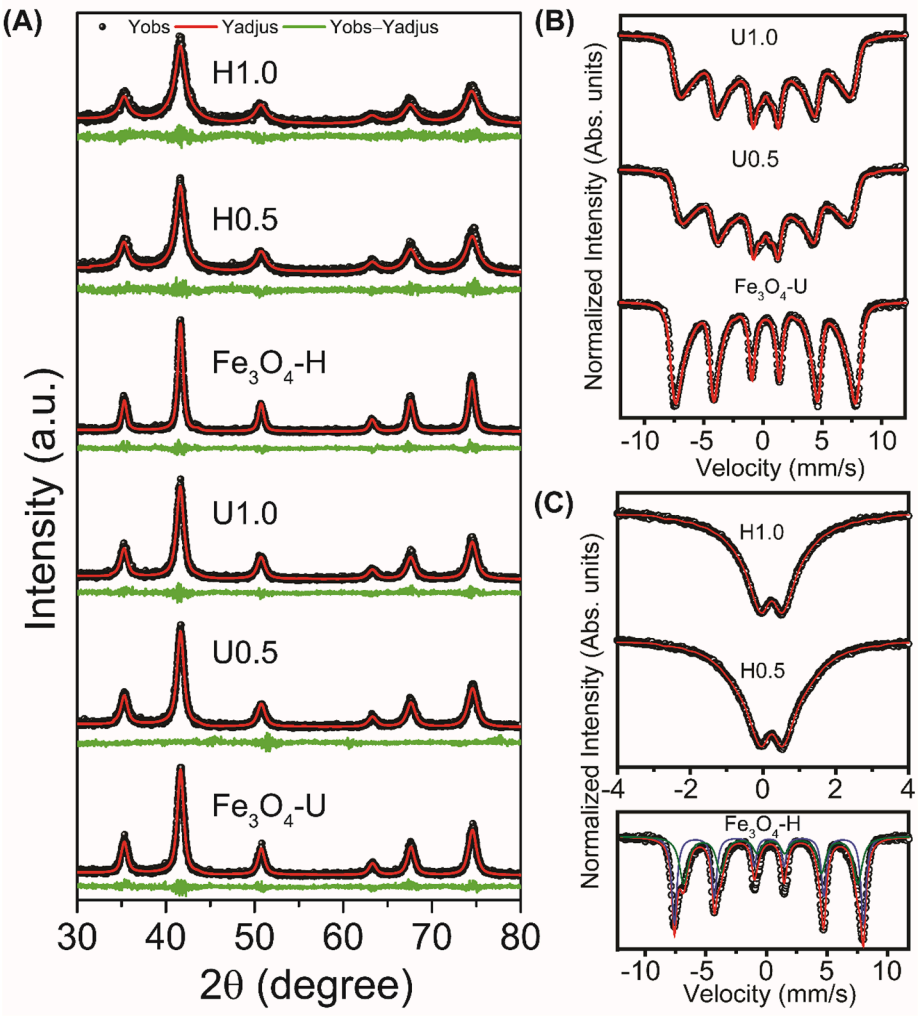

Fig. 1. (A) XRD patterns of the as-synthesized NPs. Red lines are the diffractogram adjusted according to Rietveld refinement and green lines are subtraction between observed and adjusted data. (B) MS spectra of the DTPMP-coated NPs synthesized by the sonochemistry approach and (C) DTPMP-coated NPs synthesized by the hydrothermal approach. For the sample H-Fe_3O_4 the green and blue lines are the site distributions for the populations of Fe atoms at octahedral and tetrahedral sites, respectively. (For interpretation of the references to colour in this figure legend, the reader is referred to the web version of this article.)

Table 1
Structural and magnetic parameters from XRD Patterns (through Rietveld Refinement), TEM, VSM (300 K) and ZFC-FC analysis.

Sample	XRD		TEM		VSM (300 K)			ZFC/FC				
	a (Å)	D_{XRD} (nm)	D_{TEM} (nm)	PDI_{TEM}	M_S (emu/g)	H_C (Oe)	M_r (emu/g)	T_{MAX} (K)	$<T_B>$ (K)		% Area	
									P1[a]	P2[b]	P1	P2
U1.0	8.357	10.9 ± 0.2	10.4 ± 3.1	0.30	60.8	10.7	–0.16	196.7	30.5	63.3	47.6	52.4
U0.5	8.357	10.7 ± 0.2	10.2 ± 3.9	0.38	65.0	11.0	–0.17	–	71.1	106.9	49.5	50.4
Fe_3O_4-U	8.359	12.0 ± 0.2	–	–	–	–	–	–	–	–	–	–
H1.0	8.369	7.2 ± 0.1	8.7 ± 2.3	0.26	64.3	10.5	0.025	131.5	12.1	59.8	19.0	81.0
H0.5	8.358	7.8 ± 0.1	8.2 ± 2.6	0.31	64.2	10.6	– 0.050	171.6	62.2	89.5	71.2	24.9
Fe_3O_4-H	8.369	14.8 ± 0.3	–	–	–	–	–	–	–	–	–	–

[a] and [b]: particles population1 and 2, respectively.

[52], which is characteristic of Fe_3O_4 and γ-Fe_2O_3 oxidative like-form, being classified as isostructural phases.

Cubic cell lattice parameter (a) of the samples were 8.357, 8.357, 8.359, 8.369, 8.358 and 8.369 Å for U1.0, U0.5, Fe_3O_4-U, H1.0, H0.5, and Fe_3O_4-H, respectively, as shown in Table 1. Regarding the profile of the XRD peaks, all samples exhibited narrow and well-defined peaks, evidencing high crystallinity, unless for samples H1.0 and H0.5, which presented broader FWHM values (data not shown). Furthermore, crystallite size of the samples was calculated by Scherrer equation (see Table 1) using the data extracted from Rietveld refinement. The corresponding values for the samples U1.0, U0.5, Fe_3O_4-U, H1.0, H0.5, and Fe_3O_4-H were 10.9 ± 0.2, 10.7 ± 0.2, 12.0 ± 0.2, 7.2 ± 0.1, 7.8 ± 0.1 and 14.8 ± 0.3 nm, respectively.

3.1.2. Mössbauer spectroscopy

Mössbauer spectroscopy (MS) is a key technique in the study of magnetic materials, once MS spectrum shows information regarding their structure, electronic and magnetic properties [53]. MS spectra for all samples synthesized by sonochemistry approach (Fig. 1B) showed broadened ferrimagnetic sextets. Herein, a magnetic hyperfine field distribution was used to fit measured spectra. In the spectra profile of the samples U0.5 and U1.0 were observed a significant change in comparison to Fe_3O_4-U sample, where the sextets were broader for functionalized samples (See Fig. 1B). Indeed, a considerable change was also

evidenced in the magnetic hyperfine field (B_{hf}) distribution as a consequence of the functionalization with DTPMP (Figure S1A). For Fe_3O_4-U sample, the peak with highest intensity is centered at 47 T, whereas it appears at 45 and 44 T for U1.0 and U0.5, respectively. Moreover, the samples U1.0 and U0.5 exhibited peaks centered in 3 and 14 T, which may be observed in low intensity or absent in the distribution of the uncoated Fe_3O_4 NP sample. Additionally, the average isomeric shift (δ) was calculated for samples prepared by sonochemistry, showing values around 0.34 ± 0.02, 0.33 ± 0.02 and 0.33 ± 0.02 mm s^{-1} for U1.0, U0.5 and Fe_3O_4-U, respectively.

Interestingly, for samples prepared *via* hydrothermal method, it was observed a completely different MS spectra profile, as seen in Fig. 1C, in comparison to those synthesized by sonochemistry. A broader adsorption line composed by a quadrupole doublet was evidenced for the samples H0.5 and H1.0. In this sense, a hyperfine quadrupole splitting (*QS*) distribution was used to fit measured spectra (Figure S1B). For the samples H1.0 and H0.5, the peaks of the *QS* distribution are centered in 0.6 and 0.5 mm/s, respectively.

In contrast, the uncoated Fe_3O_4-H sample exhibits two ferrimagnetic sextets, which are assigned to the Fe atoms at the octahedral (green sub-spectrum) and tetrahedral (blue sub-spectrum) environments of Fe_3O_4 (Fig. 1C – bottom spectrum). The hyperfine parameters calculated from the site distribution fit are shown in Figure S1C, and the obtained values are in agreement to other Fe_3O_4 NPs synthesized by hydrothermal method [54].

3.1.3. TEM

We performed a TEM analysis aiming to acquire information concerning morphology, size and structure of the DTPMP-coated NPs. TEM micrographs are shown in Fig. 2A–D. The average particle diameter (D_{TEM}) and the calculated polydispersity index (PDI_{TEM}) values obtained by TEM images are listed in Table 1. Size distribution curves are presented as insets in Fig. 2. The D_{TEM} values of all samples were similar to those found through XRD data analysis (D_{XRD}). For the samples U1.0, U0.5, H1.0 and H0.5 the average diameter values were 10.4 ± 3.1, 10.2 ± 3.9, 8.7 ± 2.3 and 8.2 ± 2.6 nm, respectively, whereas, the PDI_{TEM} values were 0.30, 0.38, 0.26 and 0.31, respectively.

In general, for all synthesized NPs, TEM micrographs showed a core-type structure of a pseudo spherical morphology, which is expected when the synthesis of Fe_3O_4 NPs is performed through coprecipitation reaction of Fe^{2+} and Fe^{3+} ions using ammonium hydroxide [43,55].

For the samples U1.0 and H1.0, a core-shell like structure was observed, as signed by the red arrows in Fig. 2B and D, which can be attributed to the DTPMP coating. The average thickness values of the coating were 3.3 ± 1.7 and 14.9 ± 5.1 nm for samples U1.0 and H1.0, respectively. In Figure S2 is shown the thickness distribution curves for samples U1.0 and H1.0. In contrast, none core-shell structure was found for samples prepared with 0.5 g of DTPMP. The representative image with higher magnification of the sample U0.5 confirmed an absence of a core-shell structure, i.e. a DTPMP coating was not observed. However, magnetite crystalline planes were well-defined, indicating a good crystallinity (See Figure S3).

3.1.4. Magnetic measurements

The hysteresis loops of DTPMP-coated NPs at 300 K are shown in Figure S4, where low field curves are exhibited inset, evidencing small

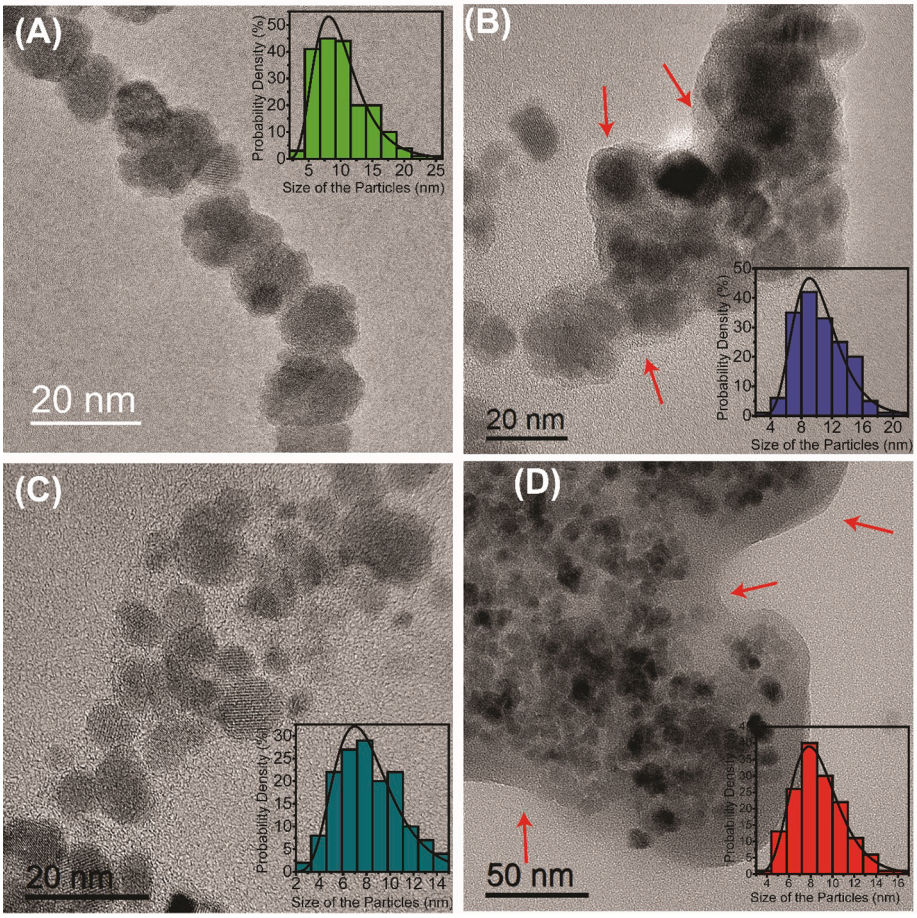

Fig. 2. TEM micrographs of the samples (A) U0.5, (B) U1.0, (C) H0.5, and (D) H1.0. Red arrows indicate the presence of a shell-like structure. Inset: Size distribution curve obtained from TEM analysis for each sample. The average diameter value for each sample is shown in Table 1. (For interpretation of the references to colour in this figure legend, the reader is referred to the web version of this article.)

hysteresis loop for all analyzed samples. From these measurements, magnetization saturation (M_S) values were calculated, as well as remnant magnetization (M_R) and coercivity (H_C). All values are summarized in Table 1.

It was observed small numerical variation for M_S and H_C parameters, comparing NPs synthesized by sonochemistry and hydrothermal methods. For example, the samples H1.0, H0.5, U1.0 and U0.5 showed M_S around 64.3, 64.2, 60.8 and 65.0 emu/g, respectively.

Magnetization curves as a function of temperature were measured under ZFC-FC conditions (Fig. 3A). All samples showed FC curve with a flat profile at low temperatures, as a consequence of the presence of dipolar interactions [43]. The blocking temperature (T_B) of magnetic NPs is defined as the crossover between superparamagnetic and ferrimagnetic states. Therefore, at T_B, sufficient energy is provided to the system and the spin is found to surpass the barrier energy, in order to perform the relaxation process towards another equilibrium position [56]. In this sense, T_B may be estimated by the maximum of the ZFC curve (T_{MAX}) [57]. Except for U0.5 sample, all other samples exhibited a maximum in ZFC, as can be seen in Table 1 for obtained T_B values.

However, it is worth to mention that this method is not completely suitable for estimate T_B, since T_{MAX} is affected by experimental parameters and size dispersion [47]. Indeed, as T_B is proportional to volume of the NPs, and, in real systems, this parameter is reasonably described by a log-normal distribution. Therefore, a more appropriate methodology would be considered T_B as a distribution in order to calculate the values closer to the real ones [47]. Thus, firstly we used the temperature derivative of the ZFC–FC difference to extract a distribution of T_B values. Then, the data could be described using a log-normal distribution. The maximum of the simulated curve was assumed to be a T_B mean ($<T_B>$), and area of a log-normal distribution was also investigated (Fig. 3B and Table 1). Furthermore, T_B distributions of synthesized DTPMP-coated NPs were better fit to two log-normal distributions, which physically means two populations of particles, as shown in the Table 1 (P1 and P2). Efforts to fit those using just one distribution were unsuccessful. As a consequence, the coefficients of determination (R^2) were not suitable. Table S1 shows the mean $<T_B>$, standard deviation of $<T_B>$, area for each distribution and R^2 for each fit.

3.2. DTPMP-coating properties

FT-IR and XPS analyses were performed in order to confirm the functionalization of DTPMP with magnetite NPs, and also evaluate coating properties regarding final material applications.

For XPS and FTIR measurements, a complex of DTPMP and Fe^{2+} and Fe^{3+} was prepared in order to observe the peak and bands relative to the chemical interaction between Fe and DTPMP molecules, labeled as DTPMP-Fe^{2+}-$Fe3^{+}$. Indeed, the regions of the spectrum of DTPMP-Fe^{2+}-$Fe3^{+}$ were then compared to DTPMP-coated MNPs spectra. In this regard, we assumed that the Fe ions complex was coordinated to phosphonate and/or amine groups.

3.2.1. XPS

The functionalized NPs were investigated regarding Fe, O and P atoms by XPS, since it is well-known as a suitable and sensitive surface technique. The survey spectra for all samples are presented in the Figure S5A-F. In Fig. 4A and B is shown the deconvoluted high-resolution XPS spectra for (A) O 1s and (B) N1s. The high-resolution spectra for Fe $2p_{3/2}$ and P2p are shown in Figure S6 A-C. Moreover, the atomic concentration at the surface (AC %), data extracted by the deconvolution, and the attributions to each sub-spectrum are shown in Table S2.

The O1s absorption showed valuable information concerning to DTPMP and Fe_3O_4 NPs interactions (Fig. 4A). For non-functionalized Fe_3O_4 NPs, three peaks were observed, 529.98, 531.42 and 533.40 eV, which are related to Fe–O from Fe_3O_4(Fe–O_{Fe3O4}), Fe–OH (Fe–OH_{Fe3O4}) and absorbed H_2O, respectively [58]. In contrast, the DTPMP-Fe^{2+}-Fe^{3+} complex exhibited two peaks centered in 531.28 and 532.84 eV, where the first one can be assigned to P–O–Fe, P = O and/or P = O···Fe (labeled P–$O_{DTPMP\text{-}Fe}$) [59,60]. Moreover, it was not attempt to differentiate the peak of Fe–OH of Fe_3O_4 from the P–$O_{DTPMP\text{-}Fe}$, for the samples functionalized with DTPMP (Fig. 4A). Thus, the spectra of the DTPMP-coated NPs were assigned with three peaks centered in 530.08, 531.39 and 533.94 eV. The peak of highest intensity shifted to values slightly smaller than those of the DTPMP complex. Additionally, the ratio between the area of the peaks P–$O_{DTPMP\text{-}Fe}$ (Fe–OH_{Fe3O4} for uncoated Fe_3O_4) and Fe–O_{Fe3O4} were 0.34, 0.49, 0.47, 0.66 and 0.76 for the

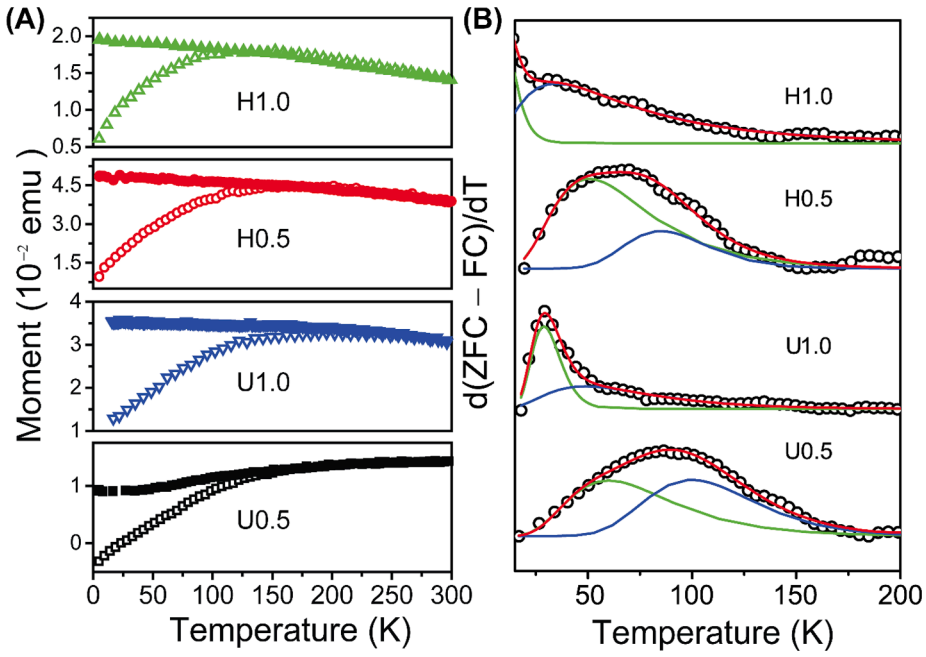

Fig. 3. (A). ZFC and FC magnetization curves Solid dots represent FC curves and open dots represent ZFC curves. (B) Log-normal fit of the d(ZFC–FC)/dT derivative for the DTPMP coated NPs. Population 1: green distribution; Population 2: blue distribution. (For interpretation of the references to colour in this figure legend, the reader is referred to the web version of this article.)

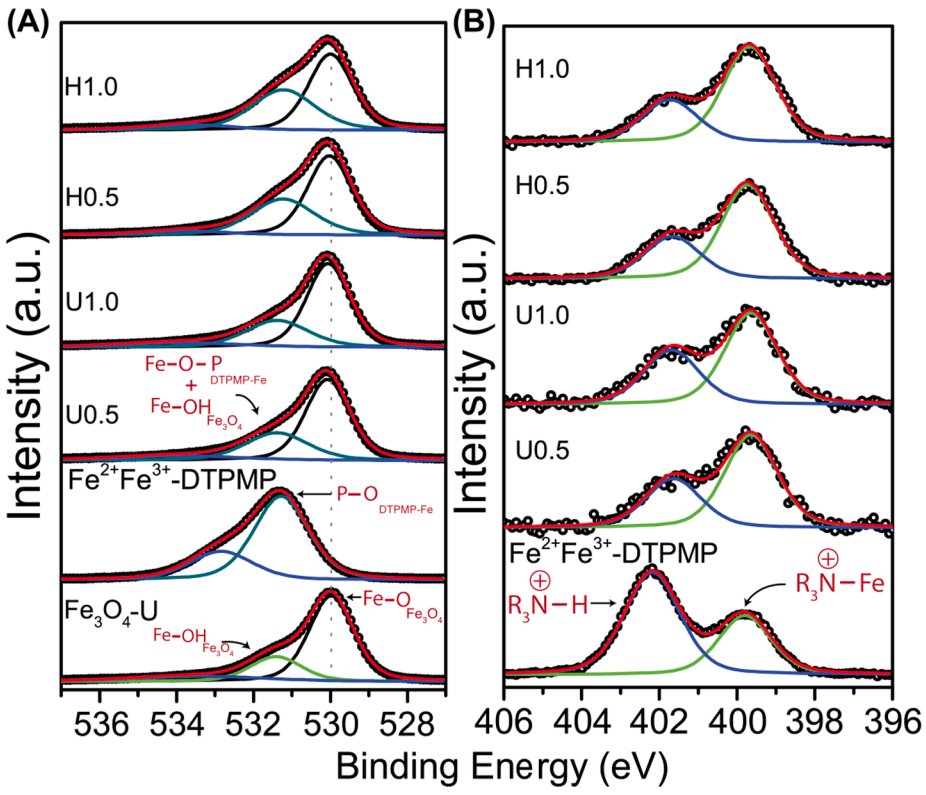

Fig. 4. Deconvoluted high-resolution XPS spectra for (A) O1s and (B) N1s of all synthesized samples. The most important attributions for each sub-spectrum are shown in this Figure. The attributions for all sub-spectra are shown in Table S2.

samples Fe_3O_4-U, U0.5, U1.0, H0.5 and H1.0, respectively (Table S2).

Relevant information concerning to DTPMP and Fe_3O_4 surface interactions can also be extracted from the high-resolution N1s spectra (Fig. 4B). A broad peak was detected for all samples, fitted into two components, 399.7 and 401.7 eV, where the first peak is attributed to amine groups from DTPMP bonded to Fe atoms from Fe_3O_4 (R_3N^+–Fe), and the second was assigned to protonated amine groups from DTPMP (R_3N^+–H) (Fig. 4B and Table S2) [61–63]. The peak at 399.7 eV is mainly attributed to the amine groups bonded to Fe atoms due to the presence of this peak in the complex sample DTPMP-Fe^{2+}-$Fe3^+$, and according to the literature, nitrogen atoms from DTPMP participate in the coordination to iron atoms in DTPMP-Fe complex [64]. Interestingly, the R_3N^+–Fe peak was more intense for functionalized NPs in comparison to R_3N^+–Fe for DTPMP-Fe^{2+}-Fe^{3+} complex (Fig. 4B).

Information concerning the number of amine groups bonded to the surface can be extracted from the ratio between the area of R_3N^+–Fe ($A_{R3N+-Fe}$) and R_3N^+–H (A_{R3N+-H}). The ratio ($A_{R3N+-Fe}/A_{R3N+-H}$) values were 0.55, 1.80, 1.59, 2.10 and 2.14 for the samples DTPMP-Fe^{2+}-$Fe3^+$, U0.5, U1.0, H0.5 and H1.0, respectively. In regard to the absorption of P2p, the spectra were adjusted with two peaks, $P2p_{3/2}$ (lowest binding energy) and $P2p_{1/2}$ (highest binding energy). Additional peaks were not evidenced for DTPMP-coated NPs, in comparison to DTPMP-Fe^{2+}-$Fe3^+$ complex (Figure S6C). However, spectra of functionalized NPs presented a shift towards small binding energies (Figure S6C). The AC values of P on the surface of the NPs were 3.57, 3.86, 4.41 and 4.79% for the samples U0.5, U1.0, H0.5 and H1.0, respectively (Table S2).

3.2.2. FT-IR

Regarding FT-IR vibrational modes relative to the core material, all samples presented two bands between 400 and 800 cm^{-1} (Figure S7) [52], attributed to stretching vibrations of Fe–O bond (ν_{Fe-O}) in tetrahedral and octahedral sites. The samples Fe_3O_4-U, U0.5, U1.0, H0.5 and H1.0 presented ν_{Fe-O} bands centered in 561, 584, 588, 588 and 584 cm^{-1}, respectively.

Concerning the bonding mechanism between Fe_3O_4 NP surface and DTPMP, FT-IR has been shown to be a suitable technique, specifically for phosphonate groups, through the analysis of a set of vibrational modes located between 850 and 1210 cm^{-1} [26,59,65–68], as shown in Fig. 5A. Regarding the binding of phosphate groups and iron oxides, Barja *et al.* reported three possibilities through the systematic study of the complexation of methylphosphonic acid with goethite particles, such as protonated monodentate complex [R–PO(OH)(O–Fe)], bridging bidentate complex [R–PO(O–Fe)$_2$] and deprotonated monodentate complex [R–P(PO_2)(O–Fe)] [65]. Additionally, Demin *et al.* also considered a tridentate complex form [R–P(O–Fe)$_3$] [66].

In this work, the bonded mechanism is proposed considering all above complex-form possibilities, in which we performed a spectral deconvolution of FT-IR spectra for the region of interest, as shown in Fig. 5A. The attribution to each sub-spectrum is in Table S3. It was considered, in the spectral deconvolution, vibrational modes relative to four chemical groups, as shown in Fig. 5B. The main chemical groups considered into discussion were: phosphoric acid groups anchored to the Fe atoms as protonated monodentate complex (*a′*), presenting stretching of the groups P–OH, P–OFe and P=O (ν_{P-OH}, ν_{P-O-Fe} and $\nu_{P=O}$ – Fig. 5B a′); phosphoric acid groups anchored to the Fe atoms as bridging bidentate complex (*a″*), presenting symmetrical and asymmetrical stretching of the groups P–OFe ($\nu_{s\ P-O-Fe}$ and $\nu_{a\ P-O-Fe}$) and P=O ($\nu_{P=O}$), as shown in Fig. 5B a″; tertiary amine groups bonded to Fe atoms (*b*) with stretching of C–N (ν_{C-N}) (Fig. 5B b); free phosphoric acid groups (*c*) presenting ν_{P-OH} as well as symmetrical and asymmetrical stretching of P–O ($\nu_{s\ P-O}$ and $\nu_{a\ P-O}$). All above mentioned groups are inserted in the spectral deconvolution vibrational modes in Fig. 5A.

For DTPMP-Fe^{2+}-$Fe3^+$ sample, the bond between phosphoric acid groups and Fe atom are characterized by the presence of the following stretching vibrational modes: ν_{P-OH} (936 cm^{-1}), ν_{P-O-Fe} (1004 cm^{-1}) and $\nu_{P=O}$ (1183 cm^{-1}) (Fig. 5A a′), which can be related to a protonated monodentate complex [65]. It was also evidenced in 1079 cm^{-1} stretching vibrations for C–N–Fe groups, which is supported by XPS

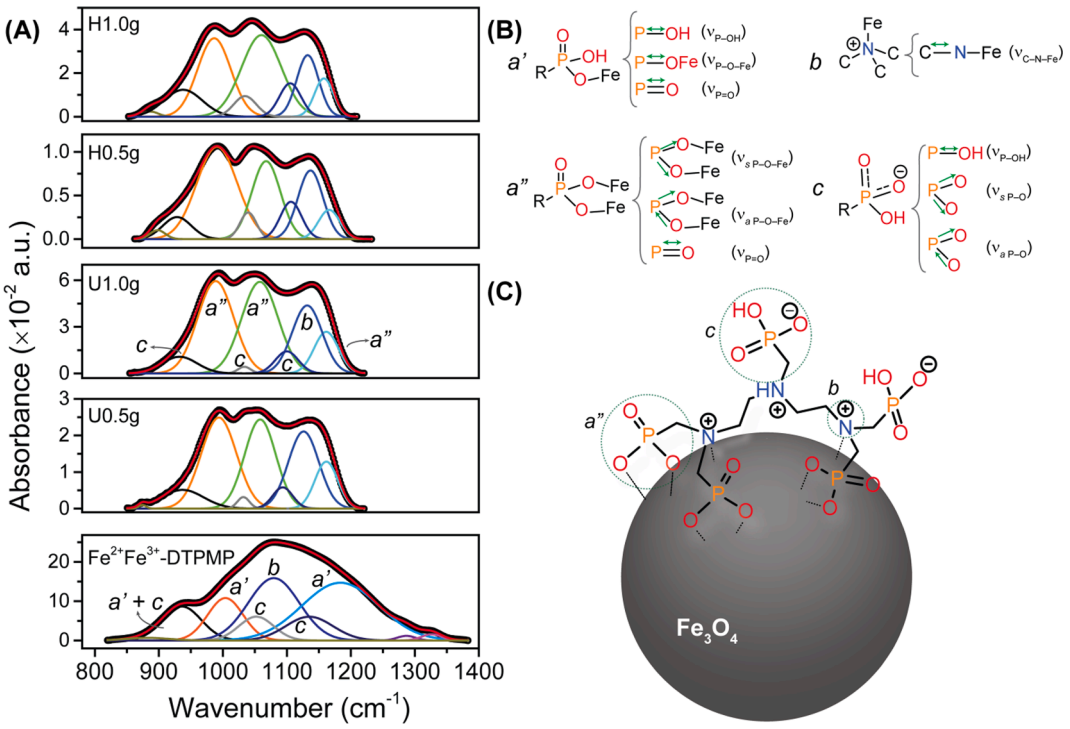

Fig. 5. (A) Deconvoluted FTIR spectra of the region of interest for the elucidation of the mechanism of bonding between Fe_3O_4 NPs and DTPMP. (B) Schematic illustration for main vibrational modes, considering deconvolution spectral. (C) The proposal of bonding between Fe_3O_4 NPs and DTPMP molecule. Attributions of each sub-spectrum are shown in Table S3. Small letters (*a′*, *a″*, *b* and *c*) represent the sub-spectrum relative to each chemical group presents in DTPMP-coated MNPs.

results (Fig. 5A b) [69]. Regarding free phosphoric acid groups, which were in the form of R–PO_3H^-, we detected three vibrational modes: $\nu_{P–OH}$ (883 and 936 cm^{-1}), $\nu_{a\ PO2}$ and $\nu_{s\ PO2}$ (1052 and 1135 cm^{-1}, respectively) (Fig. 5A c) [65].

For DTPMP-functionalized MNPs, we evidenced the same bands observed in the complex for the bonding between nitrogen and iron as well as free phosphoric acid groups (Fig. 5A-B b and c). However, phosphoric acid groups were anchored onto the surface through bridging bidentate form, due to the presence of the following vibrational modes: $\nu_{s\ P–O–Fe}$, $\nu_{a\ P–O–Fe}$ (989 and 1100 cm^{-1}, respectively) and $\nu_{P=O}$ (1161 cm^{-1}) (Fig. 5A-B a″) [65,70,71]. Based on these results, we proposed the model of interaction between DTPMP and Fe_3O_4 NPs as shown in Fig. 5C.

3.3. Colloidal properties

The nanoparticles exhibited a magneto-fluid response in water after DTPMP functionalization, i.e. if a magnet bar is placed close to the colloidal dispersion, the fluid is attracted to the magnet as whole, and no separation between dispersed nanoparticles and liquid phase is observed (See Supported Video). Actually, this behavior is an additional evidence of the success of the functionalization step, as well as the good colloidal stability.

In-depth, the hydrodynamic properties of the aqueous dispersions of the coated-MNPs were evaluated by DLS in three different solvents: deionized water, phosphate buffer 7.4 (PB 7.4) and phosphate buffer saline 7.4 (PBS 7.4). They were selected due to their biological relevance. All samples were measured in terms of hydrodynamic size, polydispersity index (PDI_{DLS}) and zeta potential (ζ), as shown in Table 2. In both buffer dispersions, the hydrodynamic size for all samples did not increase in comparison to deionized water NPs dispersion. All size distributions curves exhibited unimodal behavior (Figure S8-11). Interestingly, for the NPs synthesized by sonochemistry, the PDI_{DLS} values increased when the samples were dispersed in physiological solutions, whereas the opposite behavior occurred for samples obtained by hydrothermal route. It is worth mentioning that the Z-average size values were around 15 times bigger than the average particles diameter calculated by XRD and TEM, potentially indicating cluster formation in aqueous environment.

The ζ is an important parameter to be analyzed regarding colloidal

Table 2
Hydrodynamic particle size, surface charge and PDI obtained by DLS in different aqueous solvents.

Sample	Solvent	Hydrodynamic diameter (nm)	PDI_{DLS}	ζ (mV)[a]
U1.0	H_2O	149.1 ± 0.7	0.101 ± 0.020	–31.3 ± 0.51
	PB 7.4	124.1 ± 0.7	0.140 ± 0.012	
	PBS 7.4	133.5 ± 2.4	0.310 ± 0.031	
U0.5	H_2O	151.4 ± 1.3	0.086 ± 0.026	–36.0 ± 1.10
	PB 7.4	127.3 ± 1.3	0.149 ± 0.007	
	PBS 7.4	123.1 ± 1.0	0.201 ± 0.020	
H1.0	H_2O	142.9 ± 0.8	0.247 ± 0.006	–28.0 ± 1.99
	PB 7.4	131.0 ± 0.9	0.205 ± 0.009	
	PBS 7.4	125.5 ± 0.5	0.199 ± 0.010	
H0.5	H_2O	125.3 ± 1.0	0.212 ± 0.007	–33.2 ± 0.88
	PB 7.4	135.7 ± 1.2	0.275 ± 0.006	
	PBS 7.4	117.0 ± 1.0	0.214 ± 0.006	

[a] pH around 6.5.

suspensions, once it gives a clear magnitude and nature of the surface electric charge. All evaluated samples showed surface charge values between –28.0 ± 1.99 and –36.0 ± 1.10 mV (Table 2), mainly related to the de protonation of the phosphonic acid groups from DTPMP.

In order to have a deeper understanding of the surface properties of DTPMP-coated NPs, ζ and Z-average size were measured as a function of pH (Fig. 6A and B). The sample U1.0 was selected as a model once this sample exhibited a greater performance as MRI contrast agent. In acid medium (pH in the range of 3–4), the ζ showed positive values due to the protonation of the tertiary amine groups from DTPMP on particles surface. At pH values higher than 4.08, which is the isoelectric point (IEP) of DTPMP, it was observed negative values of surface charge. At pH 10, the ζ reached a minimum of –32.5 mV.

Hydrodynamic size followed similar profile, where values close to IEP, the samples exhibited highest size values. It is known that the absence of electric charge on the surface causes the attractive forces of Wander-Walls, in order to overcome the repulsive electrostatic force, leading to aggregation of the particles and higher hydrodynamic size values. This behavior is confirmed through the macroscopic colloidal stability, as shown in Fig. 6B. For instance, in Fig. 6B – point II, when the colloidal suspension of DTPMP-coated MNPs reaches pH 4, the NPs precipitate, and as the pH increases, the NPs become dispersed (Fig. 6B – Point III and IV).

3.4. Cytotoxicity evaluation

For MRI contrast agent application, a preliminary evaluation of the DTPMP-coated NPs on human neutrophils viability must be performed. In this work, two cytotoxicity tests were used, LDH activity and MTT assay.

In LDH assay, none of coated samples showed significant increase in the enzymatic activity in comparison to control group (Fig. 7A). However, the addition of Triton X-100 0.2% (w/v) (positive control) significantly increased the LDH activity in the extracellular medium. Within this context, and considering greater relaxivity properties, cell viability by MTT test was performed for the sample U1.0, in order to evaluate other cell function effects (Fig. 7B). The addition of U1.0 sample at 10, 50 and 100 μg/mL on human neutrophils suspension did not present a significant reduction in cellular viability (97–116% of viable cells) when compared to vehicle group/control group (100% of viable cells). Indeed, the percentage of viable cells in the HBSS group (medium cell culture) was similar to vehicle group (data not shown).

3.5. Magnetic resonance imaging properties

MNPs with average diameter around 7–20 nm are traditionally considered as T_2 contrast agents in MRI, as can provide a dark contrast when MR images are acquired under T_2-weighted sequences [5]. For magnetic nanoparticles, the dark (hypointense) contrast generated by T_2-contrast agents is a result of the interaction between microscopic magnetic field inhomogeneities caused by the NPs and hydrogen atoms. This interaction shortens the T_2 of the protons in their vicinities [72]. Agar 0.5% (w/v) was selected as solvent for the phantom imaging experiments instead of deionized water [73], in order to better simulate the T_2 signal of living tissues, since relaxivity properties of this gel are well-described and frequently used as MRI phantoms reference [74].

The efficiency of a nanomaterial dispersion as a T_2-contrast agent for MRI is evaluated in terms of transverse relaxivity (r_2) and the ration between r_2 and longitudinal relaxivity (r_1) – r_2/r_1. These parameters can be evaluated by preparing MNPs dispersions at different dilutions, and further measuring the relaxation time (T_2 and T_1) for each dispersion. Finally, the slope of the plot between relaxation rate (T_2^{-1} or R_2; T_1^{-1} or R_1) versus concentration of Fe (mmol L^{-1}) can be calculated [75]. The r_2, r_1 and r_2/r_1 values for the samples U0.5, U1.0, H0.5 and H1.0 are presented in the Table 3. Linear fitting between the inverse of T_1 and T_2 versus Fe concentration, are shown in Figure S12 (A–D) and Fig. 8 (A and B), respectively.

Fig. 8C and D show a T_2-weighted MR image of the phantom and a T_2 map for all prepared dispersions containing functionalized NPs. In both images, as the Fe concentration increases in the dispersion, a greater contrast is observed, e.g. as dark the contrast in T_2-weighted image as short the relaxation time in T_2 map. Additionally, in T_2-weighted image, no apparent difference was evidenced among analyzed samples. However, samples U1.0 and U0.5 induced a slightly greater shortening in T_2 in comparison to H0.5 and H1.0, as shown in T_2 map (Fig. 8D).

4. Discussion

4.1. Effect of DTPMP in the structural and magnetic properties of MNPs

In this work, the commercial DTPMP was presented as a new functionalizing agent for Fe_3O_4 NPs. For this purpose, DTPMP-coated NPs were synthesized using two different stoichiometries of capping agent (0.5 and 1.0 g), as well as two different well-established methodologies: sonochemistry and hydrothermal synthesis [42,43]. Therefore, in order

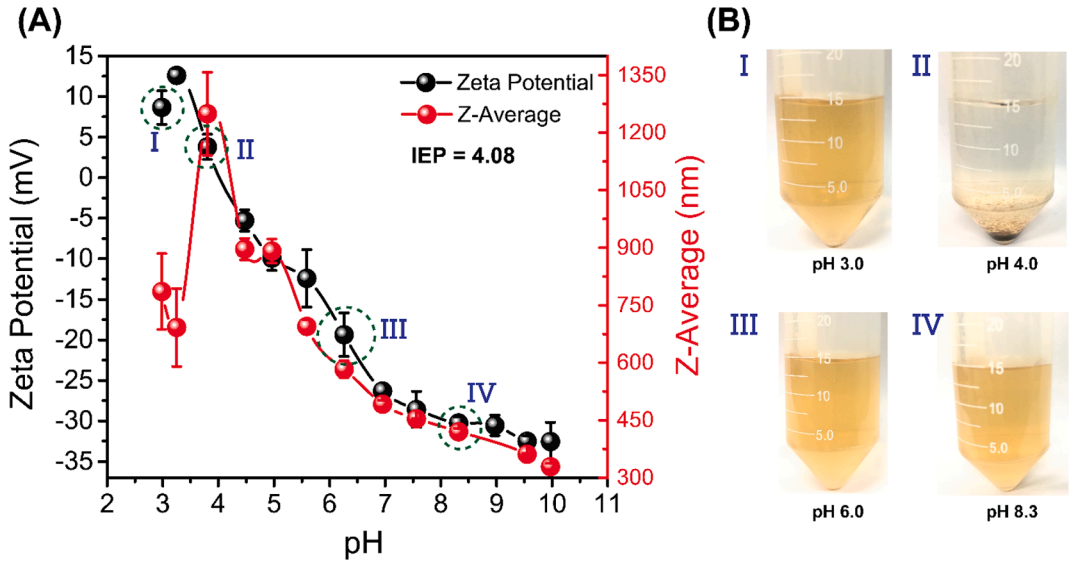

Fig. 6. (A) Influence of the pH medium in zeta potential and hydrodynamic size of the sample U1.0. (B) Images of the U1.0 suspension at different pH levels. All image samples are in equal dilution factor.

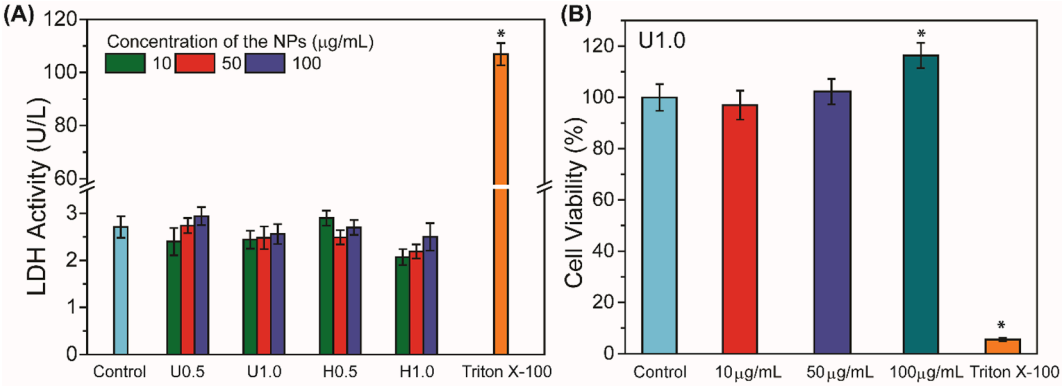

Fig. 7. Toxic evaluation of the as-synthesized NPs measured by (A) lactate dehydrogenase (LDH) activity and (B) MTT test on human neutrophils. No significant difference was found when related to the control group. ($p < 0.05$; ANOVA and Tukey's post hoc test). The results represent mean ± SEM of three separate experiments.

Table 3
Longitudinal (r_1), transversal (r_2) relaxivities and ratio r_2/r_1 for DTPMP-coated MNPs prepared in this work.

Sample	r_1 (mM s^{-1})	r_2 (mM s^{-1})	r_2/r_1
U0.5	7.39 ± 0.01	375.0 ± 0,24	50.78 ± 0.01
U1.0	8.65 ± 0.01	417.4 ± 0.3	48.25 ± 0.05
H0.5	7.98 ± 0.04	357.6 ± 0.4	44.83 ± 0.02
H1.0	9.51 ± 0.05	416.7 ± 0.2	43.81 ± 0.01

to evaluate the changes induced by DTPMP functionalization itself, a complete structural and magnetic characterization of synthesized NPs was performed aiming to understand both the effect of the amount of DTPMP on particles surface and the adopted methodologies.

XRD results indicate that NPs are composed of a single structural phase, which is related to an inverse spinal structure. This phase is characteristic of Fe_3O_4 and γ-Fe_2O_3. Additionally, cubic cell lattice parameters for our samples present values characteristic of NPs, and also intermediate values between obtained iron oxide phases (8.396 Å for Fe_3O_4 and 8.346 Å for γ-Fe_2O_3) [54,76]. Besides these values have been related to partial oxidation of Fe^{2+}, this behavior is not so far discussed herein, in-depth it is already reported in our previous work [42].

Samples U0.5 and U1.0 exhibited narrow and well-defined peaks in XRD patterns, which evidence a high crystallinity and small crystallite size for these samples. In comparison, hydrothermally coated NPs showed significant lower average crystallite size. This behavior can be related to time-addition of DTPMP, which in hydrothermal method the functionalizing agent is added in the reaction medium just after NH_4OH addition. The presence of DTPMP molecules, may hinder the growth of the MNPs and lead to smaller and poorly crystallized nanoparticles [77]

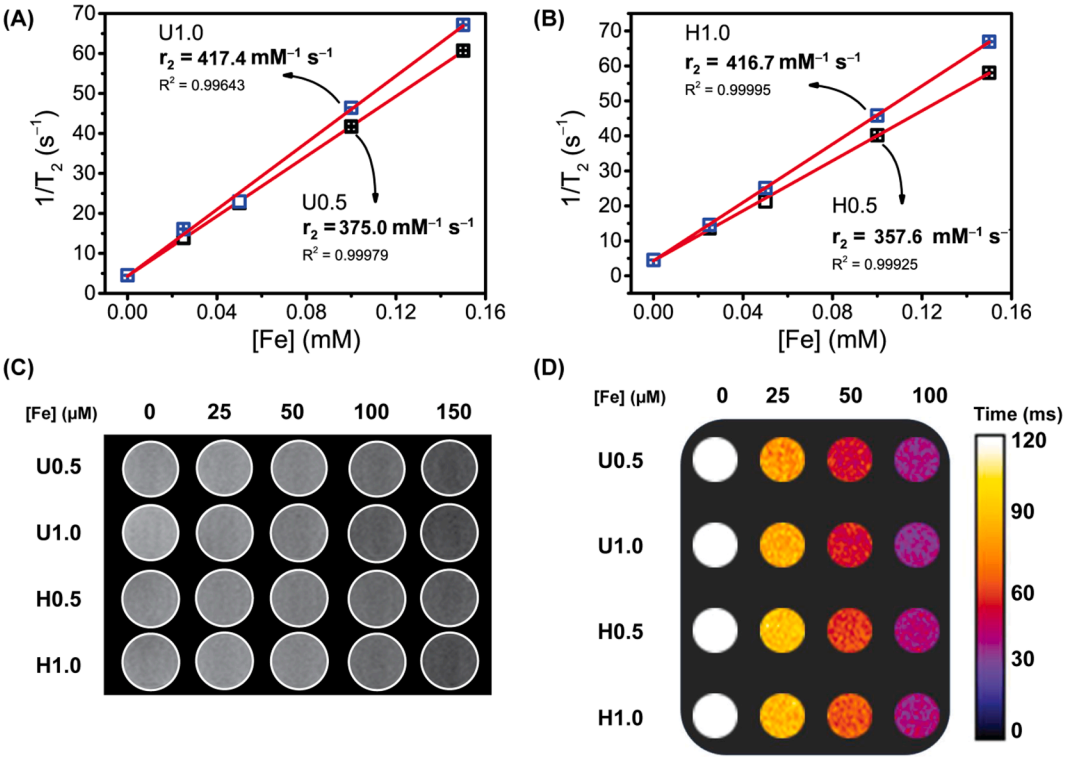

Fig. 8. Linear fittings of the inverse transversal relaxation time versus Fe concentration and r_2 relaxivity values of the samples: (A) U0.5 and U1.0 and (B) H0.5 and H1.0. (C) T_2-weighted images (fast spin echo sequence) for the DTPMP-coated magnetic nanoparticles. (D) T_2 map (multi-echo multi-slice, MEMS) sequence for the DTPMP-coated magnetic nanoparticles.

(Fig. 1A), as shown through crystallite size values obtained by Scherrer's equation and average particle diameter by TEM (Table 1).

TEM micrographs showed a core–shell structure for samples U1.0 and H1.0 (Fig. 2B and D), where the core is composed by iron oxide, as already described, and the shell mainly by organic matter. This structure-type was also evidenced for phosphonated polyethylenimine-coated magnetic nanoparticles [24]. For samples U0.5 and H0.5, the images did not show similar structure profile. Interesting, these samples also presented a thin shell since smaller quantity of DTPMP was used. In this case, during analysis, the high energy of the electron beam of TEM may have degraded the shell of these coated NPs, herein a core-shell structure was not evidencing. Additionally, for U1.0 and H1.0 samples, the organic matter-formed shell may be composed of a complex of DTPMP and Fe ions, which this hypothesis is based on the significant changes observed in the structural and magnetic properties caused by DTPMP functionalization, especially in the interparticle dipolar interactions.

MS spectra profiles and T_B values for the samples could also give a support about shell composition (Fig. 1B and C; Figure S1A and B; Fig. 3B and Table 1). Regarding to MS analysis, it is important to remember that MS spectrum of bulk Fe_3O_4 is composed by two well-defined ferri- or ferromagnetic sextets, related to Fe^{3+} in tetrahedral sites and Fe^{3+} and Fe^{2+} in octahedral sites. As the size of particles decreases, the sextets exhibit broadened lines as a result of the presence of superparamagnetic fluctuations [78]. When size decrease over the superparamagnetic critical size (25–30 nm for Fe_3O_4) leads to a broadened ferrimagnetic sextet, becoming a paramagnetic doublet [43]. However, in real systems, as MNPs interact among themselves mainly through coupling of magnetic dipole, these interactions can affect relaxation processes of the spins in MNPs. Therefore, dipole interactions can actually change the profile of MS spectra of Fe_3O_4 NPs [79].

Thus, for samples U0.5, U1.0 and uncoated-Fe_3O_4, the expected MS spectra would exhibit a paramagnetic doublet due to MNPs average size values below superparamagnetic critical size. However, when the particles exhibit dipolar interactions, broadened sextets are evidenced even for MNPs below superparamagnetic critical size [79,80]. Interestingly, for the samples U0.5 and U1.0, the spectra showed broader sextets with respect to uncoated-Fe_3O_4 (Fig. 1B), clearly indicating a decrease of dipolar interactions induced by DTPMP functionalization. Additionally, the DTPMP coating provided a significant down shift of B_{hf} of the peak of higher intensity in the B_{hf} distribution, and also induced the appearance of peaks with lower B_{hf} values (Figure S1 A). This behavior can be attributed to the increase of NPs population with smaller average diameter, where according to Witte *et al.*, the decrease in B_{hf} value can be induced by a reduction of particles size [53]. On the other hand, the presence of paramagnetic quadrupole doublet in MS spectra of the samples H0.5 and H1.0 clearly indicates a lower magnitude of dipolar interactions when compared to samples U0.5 and U1.0 (Fig. 1B and C), also supported by the decrease of particle size [53].

Concerning VSM measurements, both applied methodology of synthesis and amount of DTPMP addition did not significantly affect magnetic parameters of the MNPs (Figure S4 and Table 1). Moreover, M_S values for all samples are similar or slightly higher than those reported for functionalized Fe_3O_4 NPs synthesized by hydrothermal, sonochemistry or co-precipitation reaction route [55,81–83]. The H_C values for all samples were very similar, even for the samples H0.5 and H1.0, which showed a duplet in the MS spectra and smaller mean particle diameter when compared to the other samples. Nevertheless, small values of H_C can be related to electric currents trapped in the superconducting coil of the squid magnetometer, which induce artificial broadenings of the hysteresis loops up to 20 Oe for all samples (*inset* in Figure S4).

The amount of DTPMP effect in the dipolar interactions of DTPMP-coated Fe_3O_4 NPs was also investigated through T_B distributions (Fig. 3 B). As MNPs have great potential to be applied *in vivo*, a deeply evaluation of magnetic dipolar interactions must be performed. In general, cellular uptake assays have shown aggregates formation of MNPs in cell medium [84,85], consequently influencing their magnetic properties governed by interparticle interactions [86], as well as their signal generation [87] and heating efficiency [88]. In this regard, it is possible to correlate T_B with dipolar interactions of MNPs, considering that the increase of the strength of the dipole interaction would lead to higher T_B values [79]. This relation can be performed since the dipole interactions arise from the spin–spin coupling of different nanoparticles, and that the higher this interaction, the greater the barrier energy to occur spin relaxation. In this sense, T_B values by the maximum of ZFC curve (T_{MAX}) and temperature derivative method of the ZFC–FC difference have been measured (Fig. 3B and Table 1). These two methods generated different values of T_B, but the trend observed was the same for both. Once temperature derivative method considers aspects present in real systems, it will be consider just their values for now on.

Since the T_B distributions were adjusted by bimodal log-normal distribution, two distributions in the size distribution curves obtained by TEM would also be expected (Fig. 2A–D). However, TEM size distributions were not well adjusted with two log-normal distributions. The non-agreement in this respect between TEM size and the T_B distributions occurs because, in TEM, just a fraction of particles have their size measured (150 particles) in contrast to ZFC–FC measurements that consider a bigger population of particles. However, TEM results and T_B distributions converged for the width of the distributions. Samples U1.0 and H1.0 showed narrower T_B distributions and smaller PDI_{TEM} values, in comparison to samples U0.5 and H0.5 (Table 1 and Fig. 3B).

In Fig. 3B, it is possible to notice that the T_B distributions were significantly affected by the amount of DTPMP added during syntheses, although they exhibited the same average particle diameter, profile of MS spectra, hyperfine parameter distribution, and M_S values, as shown in Fig. 1A–C, Table 1, Figure S4). As whole, we also evidenced that the increasing of the amount of DTPMP leads to a narrower T_B distribution and smaller $<T_B>$ values, indicating that increasing the amount DTPMP a decrease of dipolar interactions is achieved. These results can be supported by TEM micrographs that indicate the presence of core shell-like structure only for U1.0 and H1.0 samples, as shown the red arrows in Fig. 2B and D. The shell of DTPMP increases the interparticle distance, which decreases spin–spin coupling and, consenquently, diminishes the dipolar interactions [89,90]. This explanation also covers the fact that H1.0 showed lower $<T_B>$ values than U1.0, once H1.0 exhibited a thicker shell-like structure (Fig. 2B and D).

4.2. Mechanism of DTPMP bonding

FTIR and XPS analyses were performed in order to confirm the functionalization, evaluating the nature of interaction between DTPMP and Fe_3O_4 surface and assigning the mechanism of bonding.

XPS spectra for all DTPMP-coated MNPs showed peaks relative to electrons of 2p orbitals of P and 1s orbital of N. In this case, the results evidence the presence of atoms only from DTPMP molecules on the surface of Fe_3O_4 (Table S2), confirming the success of the functionalization of the particles. Additionally, it is also important to notice that as the amount of added DTPMP increases, higher concentration of P and N are evidenced on the surface of Fe_3O_4, as seen in Table S2. This fact is also supported by TEM results, which showed a core-shell structure only for samples U1.0 and H1.0. Indeed, it confirms the proposed hypothesis that samples with larger amount of DTPMP have less interparticle interactions (Table 1, Fig. 3 and Table S2).

In high–resolution XPS, the spectra for N1s and O1s showed peaks with similar binding energies for complex DTPMP–Fe sample (Fig. 4 AB and B). Concerning to O1s peak, we evidenced that the samples coated with DTPMP exhibited an increase in the ratio between the area of the peaks centered in 531.30 and 530.08 eV, as a result of the contribution of the O atom in the bonds P–O–Fe, P=O and P = O···Fe [59,60,66], as seen in Fig. 4A. It is also important to notice that the peak in 531.3 eV was also evidenced in the spectrum of DTPMP–Fe complex. For N1s analysis, the spectra indicate that amine groups from DTPMP molecules

have considerable contributions to surface functionalization of Fe_3O_4, once the N1s peak centered in 399.7 eV can be attributed to amine groups anchored to iron oxide surface [61–63]. Additionally, the same peak is also observed in the spectrum of DTPMP–Fe complex. Furthermore, our results indicate that a higher number of nitrogen atoms from DTPMP molecules interacts with Fe_3O_4 NP surface in comparison to complex sample. This behavior can be evidenced regarding to the higher relative intensity of the peak in 399.7 eV (R_3N^+–Fe) in comparison to 401.7 eV (R_3N^+–H), for all coated samples (Fig. 4B). Herein, we could relate the interaction through two nitrogen atoms from DTPMP molecule bonded to Fe atoms on Fe_3O_4 NP surface. Indeed, it also supported by the ratio, approximately ~2, of relative areas of R_3N^+–Fe and R_3N^+–H peaks ($A_{R3N+-Fe}/A_{R3N+-H}$), indicating that the double of R_3N^+–Fe-form nitrogen are bonded to Fe atoms when compared to nitrogen atoms in their protonated form (R_3N^+–H) (Table S2).

To strongly validate our model of interaction between DTPMP and Fe_3O_4, we performed a FTIR spectral deconvolution in the region between 850 and 1220 cm^{-1} for DTPMP-functionalized MNPs. The proposed model was well-fitted to experimental data, giving R^2 values for all deconvolution spectra around 0.9999 (Table S3).

For the DTPMP functionalized MNPs, we inserted bands relative to three chemical groups presented in our model (Fig. 5A-C): phosphoric acid groups anchored to Fe atoms (*a″*), amine groups coordinated to Fe (*b*) atoms and free phosphoric acid groups (*c*). Concerning *a″* group, the band ~1166 cm^{-1} can be attributed to P=O, which it is not evidenced for tridentate and monodentate complex forms. Additionally, according to previous works, bands at ~1060 and 990 cm^{-1} are attributed to P–O–Fe groups [26,66–68,71], which can be assigned to asymmetrical and symmetrical vibrational modes for bidentate form, respectively. These facts indicate a bridging bidentate bonding between phosphoric acid groups from DTPMP molecules and Fe atoms from Fe_3O_4 NPs (Fig. 5 C *a″*).

Still considering the interaction between amine groups and Fe atoms (Fig. 5A-C b), we detected a vibrational mode centered at ~1100 cm^{-1} that was assigned to stretching of C–N–Fe. This attribution is considered based on the study of Lanigan *et al.*, which performed FTIR measurements of EDTA-transition metals complexes and observed a vibrational mode, ν_{C-N}, at ~1100 cm^{-1} for the coordination of tertiary amine groups to these metals [69]. Furthermore, we already evidenced ν_{C-N} at ~1100 cm^{-1} for polyethylenimine-functionalized MNPs in a previous work [42].

Vibrational modes relative to free phosphoric acid groups were also evidenced in the proposed bonding model. Indeed, after purification procedure, the pH level is around 6–7, then the phosphoric acid groups are in the form of $R–PO_3H^-$ (Fig. 5C c). Thereby, three vibrational modes were detected: symmetrical-asymmetrical PO_2 stretching and P–OH stretching. It is also important to mention that PO_2 stretching for free phosphoric acid must appear in higher wavenumber values in comparison to P–O–Fe stretching, according to Hook's law for vibration springs applied to vibrational spectroscopy [65]. Therefore, the proposal of mechanism of bonding was well-adjusted considering Hook's law (see Table S3).

After this whole discussion regarding mechanism of DTPMP bonding, it is also relevant to consider other variations of those bonding possibilities, since the exactly structure of DTPMP-functionalized Fe_3O_4 NPs could be just evaluated by aid of quantum theoretical calculations, which are beyond the scope of this work. However, it has been proved by FT-IR and XPS that the interaction between DTPMP and Fe_3O_4 NP surface occurs through both phosphate and amine groups from DTPMP molecule, providing an activated surface profile with surface-linked phosphate groups through bidentate bridges and outer free-phosphoric acid groups onto the surface of MNPs, as shown in Fig. 5C.

4.3. Surface properties of DTPMP-functionalized MNPs

As the main proposal application of MNPs is to be used in biomedicine, i.e. the site of action is inside human body, the colloidal stability in biological environment is a crucial requirement. Herein, the functionalization agent must be covalently bonding on the surface of the MNPs, and also through specific mechanisms in order to prevent particle aggregation [7]. Therefore, light-scattering measurements are a key technique in the development of this novel functionalized MNPs, since can better evaluate the behavior MNPs in aqueous suspensions.

Considering DLS results, there is a significant difference among all prepared samples for PDI_{DLS} values. Samples H0.5 and H1.0 present higher *PDI* values than U0.5 and U1.0, which indicates that hydrothermal methodology produced more polydisperse MNPs, in agreement with results reported by our group and Cai *et al.* [93] (see Table 2).

Furthermore, the synthesized samples exhibited good colloidal stability in physiological solvents, once hydrodynamic size value did not increase upon solvents dispersion. However, a significant increase in PDI_{DLS} values were observed when the samples U0.5 and U1.0 were suspended in PB 7.4 and PBS7.4, although no signal of macroscopic aggregation or precipitation of the particles was evidenced during experiments performance. Moreover, diluted samples of DTPMP-coated MNPs have shown good colloidal stability in water for more than six months.

As DTPMP molecule have both phosphoric acid and tertiary amines, it is expected that the DTPMP-coated Fe_3O_4 NPs exhibit positive and negative ζ values, depending on pH of the medium. Then, sample U1.0 was selected as a representative sample and its hydrodynamic size and ζ values were evaluated as a function of pH (see Fig. 6). At low pH values, positive ζ values were found, due to protonation of amine groups. Above pH of 4.08 (DTPMP IEP), deprotonation of phosphoric acid groups induced negative ζ values. Interestingly, the greater value of hydrodynamic size of the curve was evidenced at pH near IEP, as expected from the electrostatic stabilization mechanism of colloidal NPs. This amphoteric behavior promotes good colloidal stability at different pH, providing a versatility profile of DTPMP- covered MNPs application, principally in biosensing, catalysis, and separation media and biochemistry [37].

Interesting, considering aqueous dispersion, it is also important to observe a lower magnitude of ζ values for samples U1.0 and H1.0 in comparison to U0.5 and H0.5, as shown in Table 2. Indeed, for functionalized NPs, this behavior is expected since the ζ is the electrostatic potential at the shear plane that separates stationary layer and a mobile layer of charges in a surface charged nanoparticle, which can be affected by the NPs coating thickness [91]. For instance, according to Lowry *et al.*, for nanoparticles with larger coating thickness the imaginary shear plane is pushed outward, decreasing the overall ζ magnitude, even if the NPs have greater amount of charged molecules [92]. Herein, a similar profile was evidenced, which could be supported by TEM images of the samples U1.0 and H1.0, showing a larger coating thickness around 3.3 ± 1.7 and 14.9 ± 5.1, respectively (Fig. 2 A–D) [92].

4.4. Influence of structural, magnetic and colloidal properties on the performance of the DTPMP-functionalized MNPs as MRI contrast agent

According to the r_2/r_1 ratio value, MNCs can be classified as T_1-, T_2- and dual-type MRI contrast agent. T_1-type contrast agent has a r_2/r_1 value lower than 5, whereas r_2/r_1 values higher than 10 are classified as T_2-type, and values between 5 and 10 can be considered as dual-type contrast agent [11]. Herein, we can consider the MNCs synthesized in this work as T_2 MRI contrast agent, once we determined r_2/r_1 values of 50.78, 48.25, 44.83 and 43.81 mM^{-1} s^{-1} for the samples U0.5, U1.0, H0.5 and H1.0, respectively (Table 3).

Regarding the transverse relaxivity, our results highlighted the best performance in T_2 weighted MRI for the samples synthesized with 1.0 g of DTPMP as seen in Fig. 8A–B and Table 3. After extensive structural, magnetic and colloidal characterizations, we could certainly support this behavior.

MRI contrast agents produce contrast in the MRI exams through a

shortening (T_2 or T_1) of the relaxation time of protons from water molecules in the surroundings of the contrast agent. The interaction between the contrast agent and water molecules can happen in three different levels, with respect to the contrast agent-water molecule interface: a) inner sphere – portion, where hydrogen atoms from water (or another molecule) bind directly to the paramagnetic metal center; b) second sphere – intermediate sphere of contrast, where the contrast agent interacts with boundary hydrogen nuclei, i.e. not directly to metal center (e.g. diffusing water molecules, exchangeable protons from water molecules in the nearby environment affect the outer sphere relaxation); c) outer sphere – surrounding bulk water molecules. These portions contribute to the final relaxivity value (r_1 or r_2) [3,11]. For T_2 contrast agents, second and outer sphere are regions that promote more significantly to relaxivity values [3,11]. As a consequence, and well-reported, the T_2 relaxivity is principally affected by the size of the magnetic core and the hydrodynamic diameter and surface coating of MNPs [3,11,94]. The size of the magnetic core influences the relaxivity mainly through M_S value, since higher is the M_S more efficiently MNPs can induce field inhomogeneity and can influence a greater volume of surrounding hydrogen atoms [11].

On the other hand, when functionalized MNPs are dispersed in water, they can interact with themselves to form clusters which may have different hydrodynamic size. This parameter affects r_2 values regarding three distinctive regimes, motional average regime (MAR), static dephasing regime (SDR) and echo-limited regime (ELR). In MAR, r_2 increases with the increasing of the hydrodynamic size value, then reaches a plateau in SDR, which in this stage r_2 is independent of the hydrodynamic size. Furthermore, an increase in the hydrodynamic size leads to a decrease in r_2 (ELR) [11,95].

Regarding to the boundary hydrodynamic size for each regime, Pöselt *et al.* evidence these three regimes for polyethylenglycol-coated MNPs, and according to reported results, DTPMP-coating MNPs can be fitted between SDR and ELR regimes, core and hydrodynamic size values around 8.2–10.4 and 125–151 nm, respectively, where r_2 is maximized [95]. However, the exactly dependency of r_2 to hydrodynamic size is characteristic of each sample, and it can be mainly affected by core-size distribution and dipolar interactions.

Actually, the surface functionalization of MNPs can in-depth affects r_2. For the best of our knowledge, there is no publication reporting a systematic evaluation of the influence of the surface coating properties of MNPs considering these three cited regimes. In general, surface properties of MNPs can affect r_2 through following four manners: a) arrangement of the surface atoms – the capping agent can induce a reduction of surface spin canting, which increases M_S and consequently r_2 values [11]; b) magnetic field inhomogeneity – capping ligands rich in π-electrons can generate small local magnetic fields to an opposite direction, contributing to enhance field inhomogeneity [3]; c) interactions with water molecules – the capping agent plays an important role making water molecules diffuse closer to the magnetic core, which they can be more efficiently influenced by induced magnetic field of magnetic nanoparticles. Thus, it is desirable that the coating layer interacts with water molecules in order to increase their residence time around the magnetic core [11,94]. Therefore, It is expected that the hydrophilicity of the capping agent attached to the nanoparticles' surface plays a key role in their relaxivity properties, where more hydrophilic is the coating higher is r_2 value [96]; d) thickness – an increase in the thickness of the coating layer leads to a longer distance between hydrogen atoms and magnetic core, which decreases r_2 [11]. However, Tong *et al.* suggests that there is an optimal core-to-coating ratio which a higher content of hydrophilic coating compensates the larger distance between protons and core of the MNPs. After synthesizing PEG-coated MNPs, the authors observed that different molecular weights of PEG produced MNPs with different coating thickness, and highest value of $r_2$was achieved for – MNPs coated with intermediate value of PEG molecular weight [97].

Considering our results, as well as discussed hypothesis, samples U1.0 and H1.0 have a higher relaxivity rate due to their higher hydrophilicity surface in comparison to U0.5 and H0.5 samples. The higher hydrophilic profile of U1.0 and H1.0 are evidenced due to higher content of DTPMP on MNPs surface, which was observed by XPS and TEM analysis as seen in Fig. 2 and Table S2. Indeed, these results are in agreement with our previously work that evidenced a higher relaxivity for sodium polyacrylate-coated MNPs in comparison to branched polyethylenimine [42], once carboxylate groups promoted a higher hydrophilicity surface when compared to amine groups [98].

4.5. DTPMP-coated NPs are non-toxic for human neutrophils

Though development of new materials for medical applications the non-toxicity profile against human cells must be a crucial requirement. Within this context, cytotoxicity model tests are an important tool to select these materials with acceptable toxic effects. Herein, in this work, freshly isolated cells were used to easier evaluate the biochemical dynamics of the *in vivo* cells in the presence of DTPMP-coated MNPs [99].

Neutrophils are the most abundant leukocytes in human blood and constitute the first line of innate host defense against pathogens and associated acute inflammations [100]. Therefore, these cells are highly adequate to evaluate the safety of certain under-evaluated materials to be used through intravenous administration. According to our LDH activity assay results, DTPMP-coated NPs obtained by both sonochemistry and hydrothermal route presented as non-toxic for neutrophil plasma membrane. Additionally, since U1.0 sample showed greater medical-applied characteristics, it was investigated regarding to mitochondrial metabolic activity of human neutrophils by MTT assay [101]. As expected, no difference was observed between control group and cells treated with U1.0 at all tested concentrations, proving in-depth that magnetic nanoparticles are non-toxic for plasma membrane and/or metabolism of human neutrophils.

4.6. DTPMP-coated NPs as an alternative MRI contrast agent

As already herein reported, this work successfully shows the usage of commercial and costless compound DTPMP as a capping agent of Fe_3O_4 NPs, evaluating the potential application of this novel MNP as MRI contrast agent. Our results greatly support this intended application based on following reasons: a) high colloidal stability in physiological buffers, evidenced by dynamic light scattering experiments; b) good biocompatibility highlighted by the cytotoxicity tests, where none of the samples presented any harmful effect against neutrophils membrane or metabolic activity; c) High r_2 values confirm the potential of DTPMP-MNPs as MRI contrast agents. Indeed, r_2 values of all synthesized samples are 4 to 6 times higher than those of commercial T_2 contrast agents (References: Resovist, Feridex, and Combidex) [102,103]. Additionally, our nanoparticles have shown a better performance than other MNPs reported with similar physical-chemical properties and conventional coating agents [18,93,104,105].

Nevertheless, it is important to mention that the sample U1.0 was synthesized in just 12 min, following the sonochemistry methodology developed by our group [42], and using only water as solvent. Actually, the ultrasound technique has been shown as a versatile synthetic route methodology which was already suitable for synthesis of amine- and carboxylic acids/carboxylate-functionalized NPs, and now for aminophosphonate MNPs.

4.7. Sonochemistry vs. hydrothermal

Sonochemistry has become a remarkable synthetic route for a wide range of advanced nanomaterials, representing an ecofriendly alternative for time and energy-consuming techniques [39,106]. In this study, we used the chemical power of ultrasound irradiation itself though the well-known cavitation phenomenon, where the high energy induced by implosive collapse of cavitation bubbles could generate localized hot-spots in the liquid. Considering co-precipitation reaction under

acoustic cavitation, energy enough is released in a short reaction-time, providing ultrafast synthesis and also increasing crystallinity of nanoparticles [39]. For instance, ultrasound-assisted surface-functionalized MNPs have been reported with higher M_S values, consequently, leading to a better performance in MRI and hyperthermia applications [3,107]. In our previous work, we synthesized MNPs functionalized with carboxylate and amine groups using sonochemistry approach, which exhibited enhanced magnetic and relaxivity properties in comparison to other conventional methodologies [42]. As expected, in this currently work, we successfully obtained a novel amino-phosphonate MNP under US irradiation in just 12 min, providing a high-quality material with a potential to be applied as MRI contrast.

For comparison, we also used hydrothermal approach to prepare DTPMP-coated MNPs, which is a conventional synthetic methodology, taking the advantage of performing the synthesis of nanomaterials at temperatures well above the boiling point of the solvent (150–220 °C). It is possible to achieve these temperatures once the reaction is performed under high pressurized environment, by using a sealed high-pressure reaction vessel. The relatively high temperature should provide nanomaterials with higher crystalline [107], in comparison to those synthetic methodologies performed at smaller temperatures (25–100 °C). In this sense, it is expected that hydrothermally obtained MNPs would have higher M_S values and consequently better performance as T_2 MRI contrast agent [3]. However, we did not evidence that profile in MNPs synthesized by hydrothermal approach. Indeed, considering MRI performance, all tested samples presented similar behavior. Additionally, the samples U1.0 and H1.0 also showed other similar properties, which exhibited good colloidal stability in physiological fluids (Table 2), non-cytotoxicity to human neutrophilis (Fig. 7) and the difference in their transversal relaxivity was just 1 mM^{-1} s^{-1} (Fig. 8). The main difference was the layer thickness of the DTPMP coating (Figure S2), where U1.0 exhibited smaller and more homogeneous thickness of DTPMP coating.

Herein, by using sonochemistry approach, we could achieve a great performance as T_2 MRI contrast agent in a shorter reaction-time, around 17x faster than hydrothermal methodology. Therefore, we truly believe that the sonochemistry is a powerful synthetic approach to obtain amino-phosphonate-functionalized MNPs for MRI contrast agent, principally due to be an easy, fast and low energy cost strategy. Moreover, the novelty of this study may overcome some challenges regarding magnetic nanoparticles in clinical usage.

5. Conclusion

In summary, we successfully developed a novel phosphonate-coated material, with outstanding properties, using a commercial capping agent with affordable cost that has been underutilized in the literature. The DTPMP-coated Fe_3O_4 material was prepared through two synthetic methodologies, sonochemistry and hydrothermal approaches. Furthermore, we performed a full characterization of structural, magnetic and colloidal properties of the DTPMP-coated MNPs, which allowed us to conclude: a) increasing of the amount of functionalized DTPMP decreases the dipolar magnetic interactions in Fe_3O_4 NPs, regarding to a formation of shell-like structure for samples with more DTPMP; b) XPS and FTIR analysis confirmed that DTPMP molecule and Fe_3O_4 NPs have a chemical interaction through both amino and phosphate groups from DTPMP; c) DTPMP-coated MNPs have a magneto-fluid response characteristic of a ferrofluid; d) dynamic light scattering experiments confirmed that the surface of synthesized MNPs presents amphoteric properties. Moreover, our results also supported that this novel material has a great potential to be applied as MRI contrast agent, once exhibited colloidal stability in physiological fluids, non-cytotoxicity to human neutrophils and high value of transverse relaxivity.

It is also important to highlight that sonochemistry proved to be a more effective synthetic methodology, considering 17x faster reaction-time. Actually, ultrasound-assisted samples showed greater performance once exhibited similar or even better transversal relaxivity values in comparison to hydrothermal samples. Although we have only tested DTPMP-coated MNPs as MRI contrast agent, and considering their outstanding reported properties, we believe that these versatile nanoparticles could be applied in other technological applications, such as magnetic hyperthermia, separation science, catalysis and sensing.

CRediT authorship contribution statement

Davino M.A. Neto: Writing - original draft, Conceptualization, Formal analysis, Investigation, Resources, Data curation. **Luelc S. da Costa:** Investigation. **Fernando L. de Menezes:** Investigation. **Lillian M.U.D. Fechine:** Writing - review & editing. **Rafael M. Freire:** Investigation. **Juliano C. Denardin:** Investigation, Resources. **Manuel Bañobre-López:** Investigation, Resources. **Igor F. Vasconcelos:** Investigation, Resources. **Thiago S. Ribeiro:** Investigation, Formal analysis. **Luzia Kalyne A.M. Leal:** Investigation, Resources. **João A.C. de Sousa:** Investigation. **Juan Gallo:** Methodology, Investigation, Formal analysis, Investigation. **Pierre B.A. Fechine:** Supervision, Project administration, Funding acquisition, Conceptualization.

Declaration of Competing Interest

The authors declare that they have no known competing financial interests or personal relationships that could have appeared to influence the work reported in this paper.

Acknowledgments

We acknowledge the funding support from Brazilian and Chilean agencies: Funcap (PNE-0112-00048.01.00/16), CNPq (408790/2016-4), CAPES (Finance Code 001, PROEX 23038.000509/2020-82), Fondecyt project number (3170240 and 1200782) and Basal Program for Centers of Excellence, Grant FB0807 and AFB180001 CEDENNA, CONICYT. The authors acknowledge the Brazilian Nanotechnology National Laboratory (LNNano) for the use of electron microscopy and XPS facility under the projects (Proposal number for XPS analysis XPS-23248). MBL and JG acknowledge funding from ERDF (European Regional Development Fund) under the grant NORTE-45-2015-02, from the European Union's Horizon 2020 research and innovation programme under grant agreement no. 686009, and from the FCT UTAP-EXPL/NTec/0038/2017 project. We are grateful to the X-ray Laboratory, and Advanced Functional Materials Laboratory of the Department of Physics−Federal University of Ceará for the XRD and light scattering measurements. We acknowledge technical support of the researcher Lyara Freitas in cytotoxicity experiments.

Appendix A. Supplementary data

Supplementary data to this article can be found online at https://doi.org/10.1016/j.apsusc.2020.148824.

References

[1] V. Zheltova, A. Vlasova, N. Bobrysheva, I. Abdullin, V. Semenov, M. Osmolowsky, M. Voznesenskiy, O. Osmolovskaya, Fe_3O_4@HAp core–shell nanoparticles as MRI contrast agent: synthesis, characterization and theoretical and experimental study of shell impact on magnetic properties, Appl. Surf. Sci. 531 (2020) 147352–147363.

[2] S. Zhao, X. Yu, Y. Qian, W. Chen, J. Shen, Multifunctional magnetic iron oxide nanoparticles: an advanced platform for cancer theranostics, Theranostics 10 (2020) 6278–6309.

[3] D. Ni, W. Bu, E.B. Ehlerding, W. Cai, J. Shi, Engineering of inorganic nanoparticles as magnetic resonance imaging contrast agents, Chem. Soc. Rev. 46 (2017) 7438–7468.

[4] A.J. Gauger, K.K. Hershberger, L.M. Bronstein, Theranostics based on magnetic nanoparticles and polymers: intelligent design for efficient diagnostics and therapy, Front. Chem. 8 (2020) 1–7.

[5] E. Peng, F. Wang, J.M. Xue, Nanostructured magnetic nanocomposites as MRI contrast agents, J. Mater. Chem. B 3 (2015) 2241–2276.

[6] J. Wahsner, E.M. Gale, A. Rodríguez-Rodríguez, P. Caravan, Chemistry of MRI contrast agents: current challenges and new frontiers, Chem. Rev. 119 (2019) 957–1057.

[7] E. Amstad, M. Textor, E. Reimhult, Stabilization and functionalization of iron oxide nanoparticles for biomedical applications, Nanoscale 3 (2011) 2819–2843.

[8] Y. Li, H. Zhang, Fe_3O_4-based nanotheranostics for magnetic resonance imaging-synergized multifunctional cancer management, Nanomedicine 14 (2019) 1493–1512.

[9] K. Hola, Z. Markova, G. Zoppellaro, J. Tucek, R. Zboril, Tailored functionalization of iron oxide nanoparticles for MRI, drug delivery, magnetic separation and immobilization of biosubstances, Biotechnol. Adv. 33 (2015) 1162–1176.

[10] A. Farzin, S.A. Etesami, J. Quint, A. Memic, A. Tamayol, Magnetic nanoparticles in cancer therapy and diagnosis, Adv. Healthc. Mater. 9 (2020) 1901058.

[11] W. Zhang, L. Liu, H. Chen, K. Hu, I. Delahunty, S. Gao, J. Xie, Surface impact on nanoparticle-based magnetic resonance imaging contrast agents, Theranostics 8 (2018) 2521–2548.

[12] S. Jeon, B.C. Park, S. Lim, H.Y. Yoon, Y.S. Jeon, B.-S. Kim, Y.K. Kim, K. Kim, Heat-generating iron oxide multigranule nanoclusters for enhancing hyperthermic efficacy in tumor treatment, ACS Appl. Mater. Interfaces 12 (2020) 33483–33491.

[13] L. Du, W. Wang, C. Zhang, Z. Jin, G. Palui, H. Mattoussi, A versatile coordinating ligand for coating semiconductor, metal, and metal oxide nanocrystals, Chem. Mater. 30 (2018) 7269–7279.

[14] H. Unterweger, L. Dézsi, J. Matuszak, C. Janko, M. Poettler, J. Jordan, T. Bäuerle, J. Szebeni, T. Fey, A.R. Boccaccini, Dextran-coated superparamagnetic iron oxide nanoparticles for magnetic resonance imaging: evaluation of size-dependent imaging properties, storage stability and safety, Int. J. Nanomed. 13 (2018) 1899–1915.

[15] G. Wang, X. Zhang, A. Skallberg, Y. Liu, Z. Hu, X. Mei, K. Uvdal, One-step synthesis of water-dispersible ultra-small Fe_3O_4 nanoparticles as contrast agents for T_1 and T_2 magnetic resonance imaging, Nanoscale 6 (2014) 2953–2963.

[16] A.G. Leonel, H.S. Mansur, A.A.P. Mansur, A. Caires, S.M. Carvalho, K. Krambrock, L.E.F. Outon, J.D. Ardisson, Synthesis and characterization of iron oxide nanoparticles/carboxymethyl cellulose core-shell nanohybrids for killing cancer cells in vitro, Int. J. Biol. Macromol. 132 (2019) 677–691.

[17] F. Hu, K.W. MacRenaris, E.A. Waters, E.A. Schultz-Sikma, A.L. Eckermann, T. J. Meade, Highly dispersible, superparamagnetic magnetite nanoflowers for magnetic resonance imaging, Chem. Commun. 46 (2010) 73–75.

[18] F. Xu, C. Cheng, F. Xu, C. Zhang, H. Xu, X. Xie, D. Yin, H. Gu, Superparamagnetic magnetite nanocrystal clusters: a sensitive tool for MR cellular imaging, Nanotechnology. 20 (2009) 405102–405112.

[19] M.S. Amini-Fazl, R. Mohammadi, K. Kheiri, 5-Fluorouracil loaded chitosan/polyacrylic acid/Fe3O4 magnetic nanocomposite hydrogel as a potential anticancer drug delivery system, Int. J. Biol. Macromol. 132 (2019) 506–513.

[20] J.-H. Kim, S.-M. Kim, I.-H. Yoon, I. Kim, Application of polyethylenimine-coated magnetic nanocomposites for the selective separation of Cs-enriched clay particles from radioactive soil, RSC Adv. 10 (2020) 21822–21829.

[21] J. Zeng, L. Jing, Y. Hou, M. Jiao, R. Qiao, Q. Jia, C. Liu, F. Fang, H. Lei, M. Gao, Anchoring group effects of surface ligands on magnetic properties of Fe_3O_4 nanoparticles: towards high performance MRI contrast agents, Adv. Mater. 26 (2014) 2694–2698.

[22] M. Galli, B. Rossotti, P. Arosio, A.M. Ferretti, M. Panigati, E. Ranucci, P. Ferruti, A. Salvati, D. Maggioni, A new catechol-functionalized polyamidoamine as an effective SPION stabilizer, Colloids Surf. B Biointerfaces 174 (2019) 260–269.

[23] A.M. Demin, A.G. Pershina, A.S. Minin, A.V. Mekhaev, V.V. Ivanov, S.P. Lezhava, A.A. Zakharova, I.V. Byzov, M.A. Uimin, V.P. Krasnov, L.M. Ogorodova, PMIDA-modified Fe_3O_4 magnetic nanoparticles: synthesis and application for liver MRI, Langmuir. 34 (2018) 3449–3458.

[24] C. Monteil, N. Bar, B. Moreau, R. Retoux, A. Bee, D. Talbot, D. Villemin, Phosphonated polyethylenimine-coated nanoparticles: size- and zeta-potential-adjustable nanomaterials, Part. Part. Syst. Charact. 31 (2014) 219–227.

[25] C. Bordeianu, A. Parat, C. Affolter-Zbaraszczuk, R.N. Muller, S. Boutry, S. Begin-Colin, F. Meyer, S. Laurent, D. Felder-Flesch, How a grafting anchor tailors the cellular uptake and in vivo fate of dendronized iron oxide nanoparticles, J. Mater. Chem. B. 5 (2017) 5152–5164.

[26] A. Walter, A. Garofalo, P. Bonazza, F. Meyer, H. Martinez, S. Fleutot, C. Billotey, J. Taleb, D. Felder-Flesch, S. Begin-Colin, Effect of the functionalization process on the colloidal, magnetic resonance imaging, and bioelimination properties of mono- or bisphosphonate-anchored dendronized iron oxide nanoparticles, Chempluschem 82 (2017) 647–659.

[27] V. Torrisi, A. Graillot, L. Vitorazi, Q. Crouzet, G. Marletta, C. Loubat, J.-F. Berret, Preventing corona effects: multiphosphonic acid poly(ethylene glycol) copolymers for stable stealth iron oxide nanoparticles, Biomacromolecules 15 (2014) 3171–3179.

[28] T. Lam, P.K. Avti, P. Pouliot, F. Maafi, J.-C. Tardif, É. Rhéaume, F. Lesage, A. Kakkar, Fabricating water dispersible superparamagnetic iron oxide nanoparticles for biomedical applications through Ligand exchange and direct conjugation, Nanomaterials 6 (2016) 100–115.

[29] T.D.T. Nguyen, A. Pitchaimani, C. Ferrel, R. Thakkar, S. Aryal, Nano-confinement-driven enhanced magnetic relaxivity of SPIONs for targeted tumor bioimaging, Nanoscale 10 (2018) 284–294.

[30] V. Jacques, S. Dumas, W.-C. Sun, J.S. Troughton, M.T. Greenfield, P. Caravan, High-relaxivity magnetic resonance imaging contrast agents. Part 2. Optimization of inner- and second-sphere relaxivity, Invest. Radiol. 45 (2010) 613–624.

[31] P. Lebdušková, P. Hermann, L. Helm, É. Tóth, J. Kotek, K. Binnemans, J. Rudovský, I. Lukeš, A.E. Merbach, Gadolinium(iii) complexes of mono- and diethyl esters of monophosphonic acid analogue of DOTA as potential MRI contrast agents: solution structures and relaxometric studies, Dalt Trans. (2007) 493–501.

[32] E. Ruiz-Agudo, C. Rodriguez-Navarro, E. Sebastián-Pardo, Sodium sulfate crystallization in the presence of phosphonates: implications in ornamental stone conservation, Cryst. Growth Des. 6 (2006) 1575–1583.

[33] Y.-P. Zhu, T.-Z. Ren, Z.-Y. Yuan, Hollow cobalt phosphonate spherical hybrid as high-efficiency Fenton catalyst, Nanoscale 6 (2014) 11395–11402.

[34] K. Lv, J. Han, C.-T. Yang, C.-M. Cheng, Y.-M. Luo, X.-L. Wang, A category of hierarchically porous tin (IV) phosphonate backbone with the implication for radioanalytical separation, Chem. Eng. J. 302 (2016) 368–376.

[35] P. Selvakumar, B. Balanaga Karthik, C. Thangavelu, Surface and electrochemical characterization of corrosion inhibition of stainless steel in acid medium, J. Mater Environ. Sci. 5 (2014) 1750–1757.

[36] S.W.A. Bligh, C.T. Harding, A.B. McEwen, P.J. Sadler, J.D. Kelly, J.A. Marriott, Synthesis, characterization and comparative study of aminophosphonate chelates of gadolinium(III) ions as magnetic resonance imaging contrast agents, Polyhedron 13 (1994) 1937–1943.

[37] Y. Ma, L. Xing, H. Zheng, S. Che, Anionic−cationic switchable amphoteric monodisperse mesoporous silica nanoparticles, Langmuir 27 (2011) 517–520.

[38] W. Wu, C.Z. Jiang, V.A.L. Roy, Designed synthesis and surface engineering strategies of magnetic iron oxide nanoparticles for biomedical applications, Nanoscale 8 (2016) 19421–19474.

[39] H. Xu, B.W. Zeiger, K.S. Suslick, Sonochemical synthesis of nanomaterials, Chem. Soc. Rev. 42 (2013) 2555–2567.

[40] T.M. Freire, L.M.U. Dutra, D.C. Queiroz, N.M.P.S. Ricardo, K. Barreto, J. C. Denardin, F.R. Wurm, C.P. Sousa, A.N. Correia, P. de Lima-Neto, P.B. A. Fechine, Fast ultrasound assisted synthesis of chitosan-based magnetite nanocomposites as a modified electrode sensor, Carbohydr. Polym. 151 (2016) 760–769.

[41] J.S. Barbosa, D.M.A. Neto, R.M. Freire, J.S. Rocha, L.M.U.D. Fechine, J. C. Denardin, A. Valentini, T.G. de Araújo, S.E. Mazzetto, P.B.A. Fechine, Ultrafast sonochemistry-based approach to coat TiO_2 commercial particles for sunscreen formulation, Ultrason. Sonochem. 48 (2018) 340–348.

[42] D.M.A. Neto, R.M. Freire, J. Gallo, T.M. Freire, D.C. Queiroz, N.M.P.S. Ricardo, I. F. Vasconcelos, G. Mele, L. Carbone, S.E. Mazzetto, M. Bañobre-López, P.B. A. Fechine, Rapid sonochemical approach produces functionalized Fe_3O_4 nanoparticles with excellent magnetic, colloidal, and relaxivity properties for MRI application, J. Phys. Chem. C. 121 (2017) 24206–24222.

[43] Y. V. Kolen'ko, M. Bañobre-López, C. Rodríguez-Abreu, E. Carbó-Argibay, A. Sailsman, Y. Piñeiro-Redondo, M.F. Cerqueira, D.Y. Petrovykh, K. Kovnir, O.I. Lebedev, J. Rivas, Large-scale synthesis of colloidal Fe3O4 nanoparticles exhibiting high heating efficiency in magnetic hyperthermia, J. Phys. Chem. C. 118 (2014) 8691–8701.

[44] L. Bleicher, J.M. Sasaki, C.O. Paiva Santos, Development of a graphical interface for the Rietveld refinement program DBWS, J. Appl. Crystallogr. 33 (2000) 1189.

[45] X. Jin, X. Chen, Y. Cheng, L. Wang, B. Hu, J. Tan, Effects of hydrothermal temperature and time on hydrothermal synthesis of colloidal hydroxyapatite nanorods in the presence of sodium citrate, J. Colloid Interface Sci. 450 (2015) 151–158.

[46] I.A. Tiunov, M.V. Gorbachevskyy, D.S. Kopitsyn, M.S. Kotelev, E.V. Ivanov, V. A. Vinokurov, A.A. Novikov, Synthesis of large uniform gold and core – shell gold – silver nanoparticles : effect of temperature, Control 90 (2016) 152–157.

[47] I.J. Bruvera, P. Mendoza Zélis, M. Pilar Calatayud, G.F. Goya, F.H. Sánchez, Determination of the blocking temperature of magnetic nanoparticles: the good, the bad, and the ugly, J. Appl. Phys. 118 (2015) 184304.

[48] Y.M. Lucisano, B. Mantovani, Lysosomal enzyme release from polymorphonuclear leukocytes induced by immune complexes of IgM and of IgG, J. Immunol. 132 (1984) 2015–2020.

[49] L.M. Kabeya, A. Kanashiro, A.E. Azzolini, F.M. Soriani, J.L. Lopes, Y.M. Lucisano-Valim, Inhibitory effect of eight simple coumarins on the lucigenin enhanced chemiluminescence of rabbit neutrophils, Res. Commun. Mol. Pathol. Pharmacol. 111 (2002) 103–113.

[50] T. Mosmann, Rapid colorimetric assay for cellular growth and survival: application to proliferation and cytotoxicity assays, J. Immunol. Methods 65 (1983) 55–63.

[51] R.M. Freire, T.S. Ribeiro, I.F. Vasconcelos, J.C. Denardin, E.B. Barros, G. Mele, L. Carbone, S.E. Mazzetto, P.B.A. Fechine, $MZnFe_2O_4$ (M = Ni, Mn) cubic superparamagnetic nanoparticles obtained by hydrothermal synthesis, J. Nanoparticle Res. 15 (2013) 1616–1628.

[52] S.J. Iyengar, M. Joy, C.K. Ghosh, S. Dey, R.K. Kotnala, S. Ghosh, Magnetic, X-ray and Mössbauer studies on magnetite/maghemite core–shell nanostructures fabricated through an aqueous route, RSC Adv. 4 (2014) 64919–64929.

[53] K. Witte, W. Bodnar, T. Mix, N. Schell, G. Fulda, T.G. Woodcock, E. Burkel, A detailed study on the transition from the blocked to the superparamagnetic state of reduction-precipitated iron oxide nanoparticles, J. Magn. Magn. Mater. 403 (2016) 103–113.

[54] T.J. Daou, G. Pourroy, S. Begin-Colin, J.M. Greneche, C. Ulhaq-Bouillet, P. Legare, P. Bernhardt, C. Leuvrey, G. Rogez, Hydrothermal synthesis of monodisperse magnetite nanoparticles, Chem. Mater. 18 (2006) 4399–4404.

[55] T. Lu, J. Wang, J. Yin, A. Wang, X. Wang, T. Zhang, Surfactant effects on the microstructures of Fe3O4 nanoparticles synthesized by microemulsion method, Colloids Surf. A Physicochem. Eng. Asp. 436 (2013) 675–683.

[56] W.S. Galvão, D.M.A. Neto, R.M. Freire, P.B.A. Fechine, Super-paramagnetic nanoparticles with spinel structure: a review of synthesis and biomedical applications, Solid State Phenom. 241 (2015) 139–176.

[57] P. de la Presa, Y. Luengo, V. Velasco, M.P. Morales, M. Iglesias, S. Veintemillas-Verdaguer, P. Crespo, A. Hernando, Particle interactions in liquid magnetic colloids by zero field cooled measurements: effects on heating efficiency, J. Phys. Chem. C 119 (2015) 11022–11030.

[58] F.-Y. Cheng, C.-H. Su, Y.-S. Yang, C.-S. Yeh, C.-Y. Tsai, C.-L. Wu, M.-T. Wu, D.-B. Shieh, Characterization of aqueous dispersions of Fe_3O_4 nanoparticles and their biomedical applications, Biomaterials 26 (2005) 729–738.

[59] T.J. Daou, S. Begin-Colin, J.M. Grenèche, F. Thomas, A. Derory, P. Bernhardt, P. Legaré, G. Pourroy, Phosphate adsorption properties of magnetite-based nanoparticles, Chem. Mater. 19 (2007) 4494–4505.

[60] P.B. Paramonov, S.A. Paniagua, P.J. Hotchkiss, S.C. Jones, N.R. Armstrong, S. R. Marder, J.-L. Brédas, Theoretical characterization of the indium tin oxide surface and of its binding sites for adsorption of phosphonic acid monolayers, Chem. Mater. 20 (2008) 5131–5133.

[61] M.J. Incorvio, S. Contarini, X-Ray photoelectron spectroscopic studies of metal/inhibitor systems: structure and bonding at the iron/amine interface, J. Electrochem. Soc. 136 (1989) 2493–2498.

[62] Y. Wang, B. Li, Y. Zhou, D. Jia, Y. Song, CS-Fe(II, III) complex as precursor for magnetite nanocrystal, Polym. Adv. Technol. 22 (2011) 1681–1684.

[63] C.W. Jung, P. Jacobs, Physical and chemical properties of superparamagnetic iron oxide MR contrast agents: ferumoxides, ferumoxtran, ferumoxsil, Magn. Reson. Imaging. 13 (1995) 661–674.

[64] J. Oakes, C.G. van Kralingen, Spectroscopic studies of transition-metal ion complexes of diethylenetriaminepenta-acetic acid and diethylenetriaminepenta-methylphosphonic acid, J. Chem. Soc. Dalt. Trans. (1984) 1133–1137.

[65] B.C. Barja, M.I. Tejedor-Tejedor, M.A. Anderson, Complexation of methylphosphonic acid with the surface of goethite particles in aqueous solution, Langmuir 15 (1999) 2316–2321.

[66] A.M. Demin, A.V. Mekhaev, A.A. Esin, D.K. Kuznetsov, P.S. Zelenovskiy, V. Y. Shur, V.P. Krasnov, Immobilization of PMIDA on Fe_3O_4 magnetic nanoparticles surface: mechanism of bonding, Appl. Surf. Sci. 440 (2018) 1196–1203.

[67] G. Thomas, F. DEMOISSON, J. Boudon, N. Millot, Efficient functionalization of magnetite nanoparticles with phosphonate using a one-step continuous hydrothermal process, Dalt. Trans. 45 (2016) 10821–10829.

[68] C. Tudisco, V. Oliveri, M. Cantarella, G. Vecchio, G.G. Condorelli, Cyclodextrin anchoring on magnetic Fe_3O_4 nanoparticles modified with phosphonic linkers, Eur. J. Inorg. Chem. 5323–5331 (2012).

[69] K.C. Lanigan, K. Pidsosny, Reflectance FTIR spectroscopic analysis of metal complexation to EDTA and EDDS, Vib. Spectrosc. (2007).

[70] M.C. Zenobi, C.V. Luengo, M.J. Avena, E.H. Rueda, An ATR-FTIR study of different phosphonic acids in aqueous solution, Spectrochim. Acta Part A Mol. Biomol. Spectrosc. 70 (2008) 270–276.

[71] B. Basly, G. Popa, S. Fleutot, B.P. Pichon, A. Garofalo, C. Ghobril, C. Billotey, A. Berniard, P. Bonazza, H. Martinez, D. Felder-Flesch, S. Begin-Colin, Effect of the nanoparticle synthesis method on dendronized iron oxides as MRI contrast agents, Dalt. Trans. 42 (2013) 2146–2157.

[72] H. Lin, K. Liu, J. Gao, Surface Engineering to boost the performance of nanoparticle-based T1 contrast agents, Eur. J. Inorg. Chem. 2019 (2019) 3801–3809.

[73] G. Huang, H. Li, J. Chen, Z. Zhao, L. Yang, X. Chi, Z. Chen, X. Wang, J. Gao, Tunable T_1 and T_2 contrast abilities of manganese-engineered iron oxide nanoparticles through size control, Nanoscale 6 (2014) 10404–10412.

[74] A. Hellerbach, V. Schuster, A. Jansen, J. Sommer, MRI phantoms – Are there alternatives to agar? PLoS One 8 (2013) 70343–703451.

[75] T. Shin, Y. Choi, S. Kim, J. Cheon, Recent advances in magnetic nanoparticle-based multi-modal imaging, Chem. Soc. Rev. 44 (2015) 4501–4516.

[76] W. Baaziz, B.P. Pichon, S. Fleutot, Y. Liu, C. Lefevre, J.-M. Greneche, M. Toumi, T. Mhiri, S. Begin-Colin, Magnetic iron oxide nanoparticles: reproducible tuning of the size and nanosized-dependent composition, defects, and spin canting, J. Phys. Chem. C. 118 (2014) 3795–3810.

[77] J.M. Orozco-Henao, D.F. Coral, D. Muraca, O. Moscoso-Londoño, P. Mendoza Zélis, M.B. Fernandez van Raap, S.K. Sharma, K.R. Pirota, M. Knobel, Effects of nanostructure and dipolar interactions on magnetohyperthermia in iron oxide nanoparticles, J. Phys. Chem. C. 120 (2016) 12796–12809.

[78] T.J. Daou, G. Pourroy, J.M. Greneche, A. Bertin, D. Felder-Flesch, S. Begin-Colin, Water soluble dendronized iron oxide nanoparticles, Dalton Trans. (2009) 4442–4449.

[79] O. Gerber, B.P. Pichon, C. Ulhaq, J.-M. Grenèche, C. Lefevre, I. Florea, O. Ersen, D. Begin, S. Lemonnier, E. Barraud, S. Begin-colin, Low oxidation state and enhanced magnetic properties induced by raspberry shaped nanostructures of iron oxide, J. Phys. Chem. C 119 (2015) 24665–24673.

[80] L. León-Félix, J. Chaker, M. Parise, J.A.H. Coaquira, L. De Los Santos Valladares, A. Bustamante, V.K. Garg, A.C. Oliveira, P.C. Morais, Synthesis and characterization of uncoated and gold-coated magnetite nanoparticles, Hyperfine Interact. 224 (2014) 179–188.

[81] S. Srivastava, R. Awasthi, N.S. Gajbhiye, V. Agarwal, A. Singh, A. Yadav, R. K. Gupta, Innovative synthesis of citrate-coated superparamagnetic Fe_3O_4 nanoparticles and its preliminary applications, J. Colloid Interface Sci. 359 (2011) 104–111.

[82] L. Wu, C. Yang, Z. Lv, F. Cui, L. Zhao, P. Yang, Facile one-pot synthesis of different surfactant-functionalized water-soluble Fe_3O_4 nanoparticles as magnetic resonance imaging contrast agents for melanoma tumors, RSC Adv. 5 (2015) 50557–50564.

[83] R. Dolores, S. Raquel, G.-L. Adianez, Sonochemical synthesis of iron oxide nanoparticles loaded with folate and cisplatin: effect of ultrasonic frequency, Ultrason. Sonochem. 23 (2015) 391–398.

[84] C. Martinez-Boubeta, K. Simeonidis, D. Serantes, I. Conde-Leborán, I. Kazakis, G. Stefanou, L. Peña, R. Galceran, L. Balcells, C. Monty, D. Baldomir, M. Mitrakas, M. Angelakeris, Adjustable hyperthermia response of self-assembled ferromagnetic Fe-MgO core-shell nanoparticles by tuning dipole-dipole interactions, Adv. Funct. Mater. 22 (2012) 3737–3744.

[85] G. Salas, J. Camarero, D. Cabrera, H. Takacs, M. Varela, R. Ludwig, H. Dähring, I. Hilger, R. Miranda, M. del P. Morales, F.J. Teran, Modulation of magnetic heating via dipolar magnetic interactions in monodisperse and crystalline iron oxide nanoparticles, J. Phys. Chem. C. 118 (2014) 19985–19994.

[86] M. Lévy, F. Gazeau, J.-C. Bacri, C. Wilhelm, M. Devaud, Modeling magnetic nanoparticle dipole-dipole interactions inside living cells, Phys. Rev. B 84 (2011) 75480–75490.

[87] M. Lévy, C. Wilhelm, M. Devaud, P. Levitz, F. Gazeau, How cellular processing of superparamagnetic nanoparticles affects their magnetic behavior and NMR relaxivity, Contrast Media Mol. Imaging. 7 (2012) 373–383.

[88] R. Di Corato, A. Espinosa, L. Lartigue, M. Tharaud, S. Chat, T. Pellegrino, C. Ménager, F. Gazeau, C. Wilhelm, Magnetic hyperthermia efficiency in the cellular environment for different nanoparticle designs, Biomaterials 35 (2014) 6400–6411.

[89] M. Pauly, B.P. Pichon, P. Panissod, S. Fleutot, P. Rodriguez, M. Drillon, S. Begin-Colin, Size dependent dipolar interactions in iron oxide nanoparticle monolayer and multilayer Langmuir-Blodgett films, J. Mater. Chem. 22 (2012) 6343–6350.

[90] S. Fleutot, G.L. Nealon, M. Pauly, B.P. Pichon, C. Leuvrey, M. Drillon, J.-L. Gallani, D. Guillon, B. Donnio, S. Begin-Colin, Spacing-dependent dipolar interactions in dendronized magnetic iron oxide nanoparticle 2D arrays and powders, Nanoscale 5 (2013) 1507–1516.

[91] T. Luxbacher, The ZETA guide: Principles of the streaming potential technique, Ant. Paar GmbH Graz, Austria, 2014.

[92] G.V. Lowry, R.J. Hill, S. Harper, A.F. Rawle, C.O. Hendren, F. Klaessig, U. Nobbmann, P. Sayre, J. Rumble, Guidance to improve the scientific value of zeta-potential measurements in nanoEHS, Environ. Sci. Nano 3 (2016) 953–965.

[93] H. Cai, X. An, J. Cui, J. Li, S. Wen, K. Li, M. Shen, L. Zheng, G. Zhang, X. Shi, Facile hydrothermal synthesis and surface functionalization of polyethyleneimine-coated iron oxide nanoparticles for biomedical applications, ACS Appl. Mater. Interfaces 5 (2013) 1722–1731.

[94] N. Lee, T. Hyeon, Designed synthesis of uniformly sized iron oxide nanoparticles for efficient magnetic resonance imaging contrast agents, Chem. Soc. Rev. 41 (2012) 2575–2589.

[95] E. Pöselt, H. Kloust, U. Tromsdorf, M. Janschel, C. Hahn, C. Maßlo, H. Weller, Relaxivity optimization of a PEGylated iron-oxide-based negative magnetic resonance contrast agent for T_2-weighted spin-echo imaging, ACS Nano 6 (2012) 1619–1624.

[96] H. Duan, M. Kuang, X. Wang, Y.A. Wang, H. Mao, S. Nie, Reexamining the effects of particle size and surface chemistry on the magnetic properties of iron oxide nanocrystals: new insights into spin disorder and proton relaxivity, J. Phys. Chem. C. 112 (2008) 8127–8131.

[97] S. Tong, S. Hou, Z. Zheng, J. Zhou, G. Bao, Coating optimization of superparamagnetic iron oxide nanoparticles for high T_2 relaxivity, Nano Lett. 10 (2010) 4607–4613.

[98] X.-Y. Zheng, K. Zhao, J. Tang, X.-Y. Wang, L.-D. Li, N.-X. Chen, Y.-J. Wang, S. Shi, X. Zhang, S. Malaisamy, L.-D. Sun, X. Wang, C. Chen, C.-H. Yan, Gd-dots with strong ligand-water interaction for ultrasensitive magnetic resonance renography, ACS Nano. 11 (2017) 3642–3650.

[99] M.T. Teresa, P. Quintero-Ronderos, J. Castiblanco, G. Montoya-Ortíz, Cell culture and cell analysis, in: J.M. Anaya, Y. Shoenfeld, A. Rojas-Villarraga, R.A. Levy, R. Cervera (Eds.), Autoimmun. From Bench to Bedside, El Rosario University Press, Bogotá, 2013.

[100] D. Couto, M. Freitas, V. Vilas-Boas, I. Dias, G. Porto, M.A. Lopez-Quintela, J. Rivas, P. Freitas, F. Carvalho, E. Fernandes, Interaction of polyacrylic acid coated and non-coated iron oxide nanoparticles with human neutrophils, Toxicol. Lett. 225 (2014) 57–65.

[101] P. Wang, S.M. Henning, D. Heber, Limitations of MTT and MTS-based assays for measurement of antiproliferative activity of green tea polyphenols, PLoS One 5 (2010) 10202–10212.

[102] Y.-X.J.X. Wang, S.M. Hussain, G.P. Krestin, Superparamagnetic iron oxide contrast agents: physicochemical characteristics and applications in MR imaging, Eur. Radiol. 11 (2001) 2319–2331.

[103] Y.-X.J. Wang, Superparamagnetic iron oxide based MRI contrast agents: current status of clinical application, Quant. Imaging Med. Surg. 1 (2011).

[104] A. Jedlovszky-Hajdú, E. Tombácz, I. Bányai, M. Babos, A. Palkó, Carboxylated magnetic nanoparticles as MRI contrast agents: relaxation measurements at different field strengths, J. Magn. Magn. Mater. 324 (2012) 3173–3180.

[105] S. Santra, C. Kaittanis, J. Grimm, J.M. Perez, Drug/dye-loaded, multifunctional iron oxide nanoparticles for combined targeted cancer therapy and dual optical/magnetic resonance imaging, Small 5 (2009) 1862–1868.

[106] Y. Yao, Y. Pan, S. Liu, Power ultrasound and its applications: a state-of-the-art review, Ultrason. Sonochem. 62 (2020) 104722–104742.

[107] W. Wu, Z. Wu, T. Yu, C. Jiang, W.-S. Kim, Recent progress on magnetic iron oxide nanoparticles: synthesis, surface functional strategies and biomedical applications, Sci. Technol. Adv. Mater. 16 (2015) 23501–23544.